fluids

MDPI

Article

Empirical Energy Dissipation Model for Variable-Slope Three-Section Stepped Spillways Validated Through Dimensional Analysis and CFD Simulation

Luis Antonio Yataco-Pastor [1], Ana Cristina Ybaceta-Valdivia [1], Yoisdel Castillo Alvarez [2,*], Reinier Jiménez Borges [3], Luis Angel Iturralde Carrera [4], José R. García-Martínez [5,6,*] and Juvenal Rodríguez-Reséndiz [4]

1 Profesional de Ingeniería Mecánica de Fluidos, Facultad de Ciencias Físicas, Universidad Nacional Mayor de San Marcos, Lima 15081, Peru; luisantonio.yataco@unmsm.edu.pe (L.A.Y.-P.); ana.ybaceta@unmsm.edu.pe (A.C.Y.-V.)
2 Department of Mechanical Engineering, Universidad Tecnológica del Perú, Lima 15046, Peru
3 Department of Mechanical Engineering, Faculty of Engineering, Universidad de Cienfuegos "Carlos Rafael Rodríguez", Cienfuegos 59430, Cuba; rjimenezborges@gmail.com
4 Facultad de Ingeniería, Universidad Autónoma de Queretaro, Santiago de Queretaro 76010, Mexico; liturralde28@alumnos.uaq.mx (L.A.I.C.); juvenal@uaq.edu.mx (J.R.-R.)
5 Laboratorio de Control y Robótica, Facultad de Ingeniería en Electrónica y Comunicaciones, Universidad Veracruzana, Poza Rica 93390, Mexico
6 Análisis de Sistemas y Tecnologías Emergentes, Facultad de Ingeniería en Electrónica y Comunicaciones, Universidad Veracruzana, Poza Rica 93390, Mexico
* Correspondence: c19773@utp.edu.pe (Y.C.A.); romangarcia@uv.mx (J.R.G.-M.)

Abstract

Energy dissipation in stepped weirs depends on the complex interaction between geometry, flow regime, and surface aeration. The research proposes a dimensionless empirical model (RE3T) to predict the overall energy dissipation in three-section stepped weirs with variable slopes. The formulation integrates dimensional analysis based on the Vaschy–Buckingham theorem, controlled physical experimentation, and three-dimensional numerical simulations using CFD employing the RANS–SST turbulence model implemented in ANSYS CFX. Eighteen numerical simulations were performed covering seven geometric configurations and four hydraulic inlet conditions, covering slug, transitional, and skimming flow regimes. The CFD model was previously validated by comparison with a physical scale model, obtaining a discrepancy of only 0.38% in relative energy dissipation. The validated dataset was then used to calibrate an empirical multiplicative correlation composed of eight dimensionless groups associated with sectional slopes, number of steps, overall geometric ratio, and upstream Froude number. The proposed model achieved a coefficient of determination $R^2 = 0.81$, with relative errors generally less than 1% and a maximum deviation of 2.34%. The statistical indicators (RMSE, MAE, and bias) confirm the absence of significant systematic trends within the defined domain of validity. The results show that the Froude number and the slopes of the sections are the variables with the greatest influence on overall dissipation. The RE3T formulation is a physically consistent and computationally efficient predictive tool for the design and analysis of stepped weirs with variable slopes, extending the scope of traditional correlations developed for uniform slopes.

Keywords: energy dissipation; mathematical models; stepped spillways; computational fluid dynamics; Vaschy–Buckingham theorem

Check for updates

Academic Editor: Zheng-Tong Xie

Received: 24 January 2026
Revised: 6 March 2026
Accepted: 10 March 2026
Published: 13 March 2026

Copyright: © 2026 by the authors. Licensee MDPI, Basel, Switzerland. This article is an open access article distributed under the terms and conditions of the Creative Commons Attribution (CC BY) license.

1. Introduction

The dissipation of energy in hydraulic structures is a critical aspect in the design of outlet channels, spillways, and dam overflow structures. Among the various configurations developed, stepped spillways stand out due to their high hydraulic efficiency, their capacity to induce aeration, and their potential to reduce downstream erosion [1,2]. These structures promote jet breakup and the conversion of potential energy into turbulence and entrained air, thereby reducing the magnitude of the hydraulic jump and extending the service life of the structures [3].

Over past decades, significant progress has been made in the understanding of flow regimes over stepped spillways, mainly through experimental and numerical studies [4]. Pioneering investigations by Chanson [1,5] and Felder [3] laid the foundations for describing nappe, transition, and skimming flow regimes, highlighting the influence of the number of steps, chute slope, and surface roughness. Subsequently, Li et al. [6], Hamedi et al. [7], Sri Krisnayanti [8], and Villón [9] broadened the analysis of energy dissipation through physical models, examining the influence of the Froude number, step geometry, and longitudinal slope. These studies [10,11] consolidated the experimental understanding of the phenomenon, although most of them were restricted to single-slope configurations, limiting their applicability to real spillways with sections of different inclination.

In a complementary manner, Computational Fluid Dynamics (CFD) has been consolidated as an accurate tool for simulating complex flows over stepped surfaces [12–18]. Several authors have employed models based on the Reynolds-Averaged Navier–Stokes (RANS) equations with k–ε and SST turbulence closures, allowing the reproduction of pressure, velocity, and free-surface fields [19,20]. Recent investigations, such as those by Erdinc Ikinciogullari [21], Daneshfaraz et al. [22], Jahad et al. [23], and Ghaderi et al. [24], have demonstrated the capability of numerical models implemented in ANSYS CFX and FLOW-3D to represent with high fidelity the aeration, recirculation, and dissipation processes in stepped spillways.

In the search for more efficient configurations, alternative geometries have been explored, including pooled, trapezoidal, gabion, curved, and labyrinth spillways, with the aim of improving hydraulic performance [18,25]. Li, Guodong et al. [6] and Ghaderi et al. [26] analyzed trapezoidal–triangular labyrinth spillways, evidencing local improvements in energy dissipation, while Li, Shicheng et al. [27], Farooq et al. [28], and Mei et al. [29] studied structures with gabion steps or combinations of variable curvature, achieving moderate increases in hydraulic efficiency. However, these configurations still rely on constant longitudinal slopes, and their empirical analysis does not incorporate the progressive variation in the chute angle between consecutive sections, which is a key feature in long, real-world spillways with significant longitudinal development.

From an analytical perspective, the application of the Vaschy–Buckingham theorem has enabled the formulation of dimensionless equations to describe energy dissipation, specific energy, and flow parameters in stepped spillways [30,31]. Zhou et al. [32] and Daneshfaraz et al. [33] developed empirical models that relate the Froude number, stepped geometry, and relative energy loss. However, most of these formulations lack general dimensional validity and are limited to specific experimental ranges, without considering geometric variability between sections.

In this context, a knowledge gap is identified in the current literature: the absence of hydraulic and empirical models capable of describing energy dissipation in spillways with variable slopes featuring multiple stepped sections. Existing models, both experimental and numerical, are restricted to uniform slopes, simple geometries, or one-dimensional correlations, which prevents extrapolation of their results to more complex systems.

This study aims to contribute to the comprehensive understanding of this phenomenon through the investigation of a three-section stepped chute with variable slopes (RE3T), combining dimensional analysis, physical experimentation, and three-dimensional CFD simulation. This approach seeks to establish a robust methodological foundation for the formulation of dimensionless empirical models with extended validity, capable of predicting global energy dissipation in hydraulic structures with variable geometry.

The article is organized into five main sections. In Section 1, Introduction, the study situates the analysis of energy dissipation in stepped spillways within the broader context of modern dam safety and hydraulic structure design, highlighting stepped chutes as highly efficient dissipative systems and framing the development of an empirical model as a response to the limitations of existing correlations for complex, variable-slope geometries. In Section 2, Materials and Methods, the work details the methodological framework used to formulate and validate the RE3T model, including the design and instrumentation of the three-section physical model, the application of classical hydraulic energy equations, the configuration and execution of three-dimensional CFD simulations in ANSYS CFX 2025 R2 (25.2), and the use of the Vaschy–Buckingham theorem to derive the governing dimensionless groups and the functional form of the empirical correlation. In Section 3, Results, the article presents the main hydraulic outputs obtained from the laboratory experiments and the 18 numerical simulations—discharges, depths, total energies, head losses, and relative dissipation—together with the estimated coefficients of the empirical formula and the associated statistical indicators such as the coefficient of determination, root-mean-square error, mean absolute error, bias, and maximum relative error. Section 4, Discussion, interprets these results in light of previous experimental, numerical, and empirical studies on stepped spillways, emphasizing the methodological contribution of integrating physical modeling, CFD, and dimensional analysis to generalize energy dissipation estimation for three-section variable-slope chutes and discussing the sensitivity of the model to geometric parameters, flow regime, and Froude number within the defined validity domain. Finally, Section 5, Conclusions, synthesizes the key findings on the predictive capacity, robustness, and practical applicability of the RE3T empirical model for the design of stepped spillways with multiple slopes, and proposes recommendations and future research lines aimed at extending the formulation to other configurations, refining the treatment of flow regimes, and supporting the development of advanced design tools for dissipative hydraulic structures.

2. Materials and Methods

2.1. Description of the Physical Model and Instrumentation

The experimental study was conducted using a physical model of a three-section stepped chute (RE3T) constructed at the Hydraulics and Physical Models Laboratory of UNMSM (Figure 1). In addition to the stepped chute itself, the physical model included an upstream approach channel and a downstream outlet reach with a stilling basin. The upstream channel had a rectangular cross-section with a width b_1 and a length sufficient to develop a nearly uniform approach flow before the water reached the first step, thus minimizing entrance effects.

Downstream, the stilling basin and outlet channel were dimensioned so that the hydraulic jump and the main dissipation processes occurred well inside the physical model, far from the downstream boundary, ensuring that the flow at the outlet section was quasi-uniform and weakly influenced by the external discharge system.

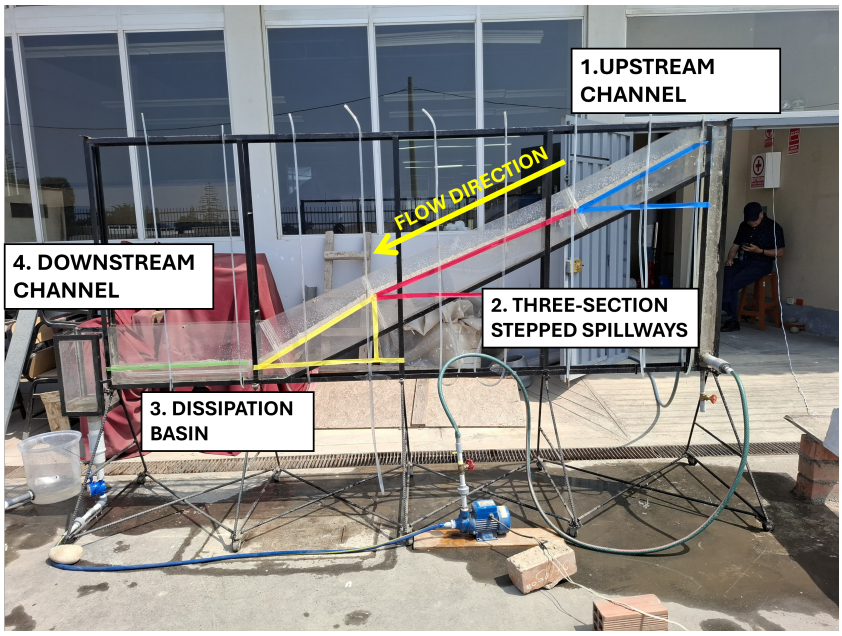


Figure 1. Physical model of a three-section stepped chute.

The precise geometric dimensions of the model were measured and verified using a vernier caliper, ensuring accurate replication of the design parameters detailed in Tables 1 and 2.

Table 1. Dimensions of the upstream and downstream zones of the stepped chute.

Zone	Width (cm)	Slope (m/m)
Upstream channel	8.10	0.0010
Downstream channel	7.80	0.0003
Dissipation basin	7.80	—

Table 2. Geometric parameters of the stepped chute (physical model).

Parameter	Section 1	Section 2	Section 3
Horizontal (cm)	2.0	2.5	1.6
Vertical (cm)	1.1	1.05	1.2
Number of steps	28	38	35
Slope (m/m)	0.55	0.42	0.75
Angle (°)	28.81	22.78	36.87
Width (cm)	8.1	8.1	8.1

Data collection was performed under rigorous control of instrumental uncertainty. The discharge was determined using the volumetric method with an error margin of ±5%, while flow depths (upstream, downstream, and conjugate depths) were measured using a precision vernier caliper with ±0.02 mm accuracy. These measurements established the baseline for numerical model validation.

2.2. Governing Equations of Energy

The calculation of energy dissipation is based on the classical equations of hydraulics. The total energy in the upstream (E_1) (Equation (1)) and downstream (E_2) (Equation (2)) control sections was determined using Bernoulli's equation as described by Chanson, H [34].

$$E_1 = z_1 + \frac{V_1^2}{2g} \quad (1)$$

$$E_2 = z_2 + \frac{V_2^2}{2g} \tag{2}$$

where g represents gravitational acceleration, and the terms z, p, and V correspond respectively to potential, pressure, and velocity heads.

In both upstream and downstream control sections, the flow is free-surface and exposed to the atmosphere; hence, the pressure head is zero and Equations (1) and (2) are evaluated using only the potential and velocity heads.

The energy loss due to the hydraulic jump (h_j) (Equation (3)) in the dissipative basin was computed using the empirical formulation for rectangular channels proposed by Villón [35]:

$$h_j = \frac{(y_2 - y_1)^3}{4y_1y_2} \tag{3}$$

where y_1 and y_2 are the smaller and larger conjugate depths, respectively. Based on these energy balances, the net head loss attributable to the chute (ΔH) (Equation (4)) and the relative dissipation (D_r) (Equation (5)) were defined as

$$\Delta H = E_1 - (E_2 + h_r + h_j) \tag{4}$$

where

h_r represents the energy loss due to friction and turbulence along the stepped or smooth chute (rapid flow section);

h_j represents the energy loss generated by the hydraulic jump in the stilling basin or dissipative structure.

$$D_r = \frac{\Delta H}{E_1} \tag{5}$$

2.3. Numerical Modeling (CFD)

2.3.1. Governing Equations and Turbulence Model

Computational Fluid Dynamics (CFD) provides a means to analyze complex hydraulic phenomena and obtain accurate predictions using numerical methods [36]. In this study, the ANSYS CFX 2025 R2 (25.2) software was used to solve the governing equations by means of the finite volume method, including continuity, Navier–Stokes, and energy equations [37]. For steady-state flow, these equations can be expressed as Equations (6)–(8):

$$\nabla \cdot (\rho \mathbf{v}) = 0 \tag{6}$$

$$\nabla \cdot (\rho \mathbf{v}\mathbf{v}) = -\nabla p + \nabla \cdot \tau + \rho \mathbf{g} + S_m \tag{7}$$

$$\nabla \cdot (\rho h_t \mathbf{v}) = \nabla \cdot (k \nabla T) + S_E \tag{8}$$

where

- S_m: Source term for momentum.
- S_E: Source term for energy.
- $\mathbf{v}$: Velocity vector.
- h_t: Total specific enthalpy.
- p: Static (thermodynamic) pressure.
- k: Thermal conductivity.
- T: Static temperature.
- ρ: Density.
- τ: Stress tensor.
- t: Time.

Turbulence modeling was based on the Reynolds-Averaged Navier–Stokes (RANS) approach, where flow variables are decomposed into mean and fluctuating components [38]. The closure of the RANS equations was achieved using the Shear Stress Transport (SST) turbulence model, which provides accurate predictions of flow separation under adverse pressure gradients.

The flow was modeled under steady-state conditions, assuming constant discharge and fixed upstream and downstream levels, consistent with the experimental configuration of the laboratory channel. Although transient simulations could in principle capture unsteady details of local recirculation, preliminary numerical tests showed negligible variations in the global energy dissipation when compared with the steady-state solution, while significantly increasing the computational cost. For this reason, a steady-state RANS formulation with the SST turbulence model was adopted as a physically consistent and computationally efficient approach for the present study.

2.3.2. Spatial Discretization and Boundary Conditions

The computational domain was discretized using an automatic mesh with a base element size of 0.0045 m and a maximum of 1 m. To ensure adequate resolution within the boundary layer, the Inflation Total Thickness technique was applied on the walls and bed (Figure 2), configuring six layers with a growth rate of 1.2 and a maximum thickness of 0.003 m. This configuration captured velocity gradients effectively while maintaining reasonable computational costs [39].

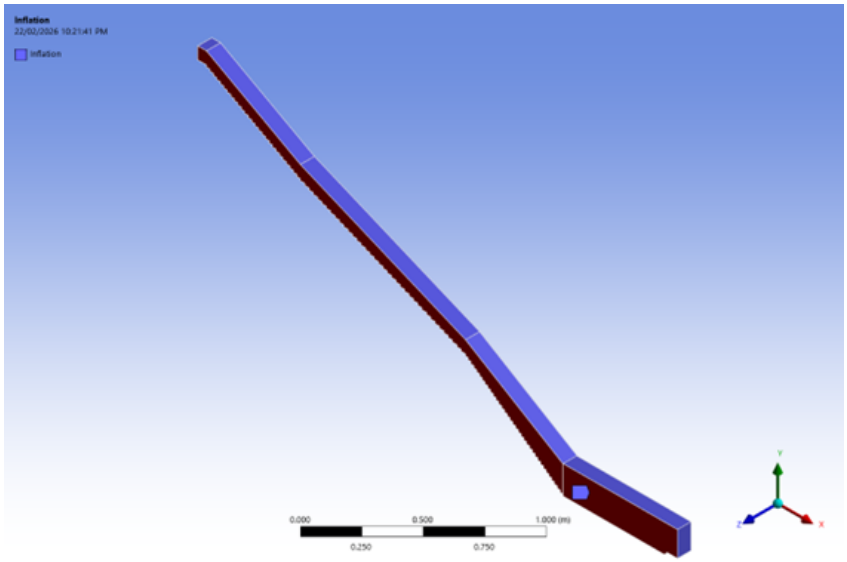


Figure 2. Boundary faces selected for the application of Inflation Total Thickness.

As shown in Figures 3–5, the longitudinal views of the computational grids (fine, medium and coarse) used in Simulation 1 illustrate the progressive refinement of the spatial discretization. The increase in element density along the stepped geometry and flow region was implemented to evaluate numerical stability and ensure mesh-independent solutions within the Grid Convergence Index (GCI) framework.

All simulations in the three-grid study were advanced up to 5000 iterations under identical hydraulic conditions, enforcing strict convergence criteria on both the residuals and the monitored hydraulic variables. The RMS residuals of continuity and momentum were required to decrease below 10^{-5}, and the time histories of upstream and downstream flow depths and total energies were tracked to ensure that no further variations occurred in the last 1000 iterations. This procedure avoided premature stabilization and guaranteed numerically converged solutions for all mesh levels.

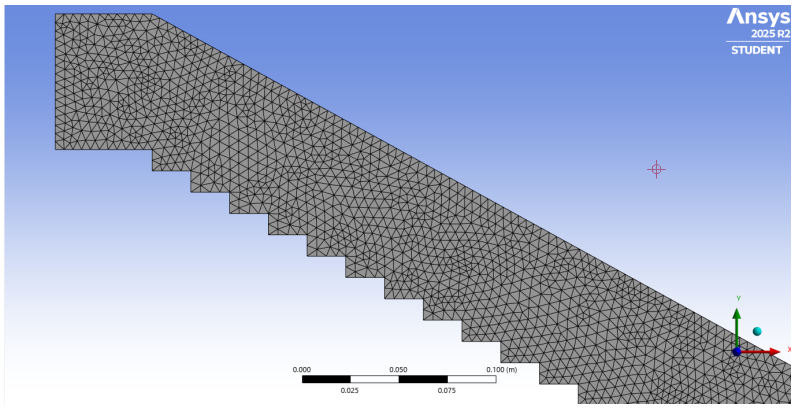


Figure 3. Wide longitudinal view of the fine mesh of Simulation 1.

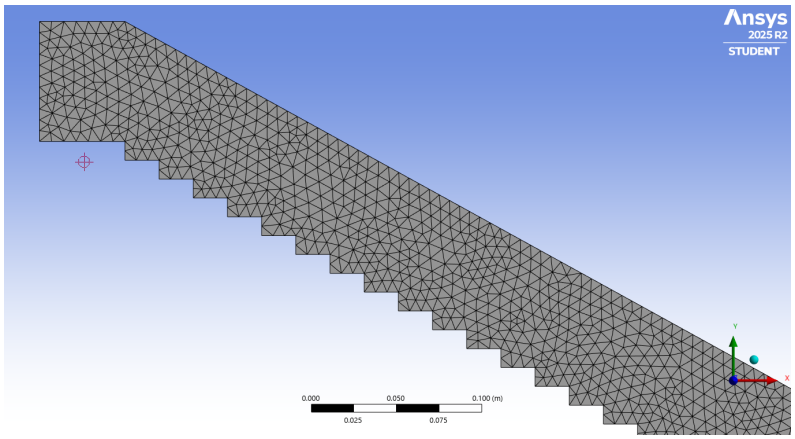


Figure 4. Wide longitudinal view of the middle mesh of Simulation 1.

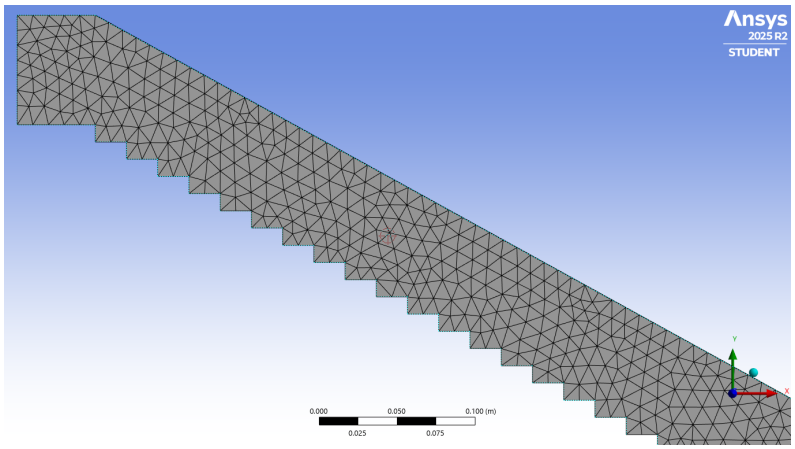


Figure 5. Wide longitudinal view of the coarse mesh of Simulation 1.

The Grid Convergence Index (GCI) methodology was applied using the upstream flow depth y_1 as the reference variable. Based on the three-grid solutions, an apparent order of convergence of $p = 6.32$ was obtained. The relative error between the fine and medium grids, ε_{21}, was found to be well below 1%.

The resulting GCI value for the finest mesh was significantly lower than 1%, confirming that the numerical solution lies within the asymptotic range of grid convergence.

Under these conditions, the fine mesh, with a base cell size of 0.0045 m and approximately 1.4×10^6 elements, was selected for all subsequent simulations.

In addition to global mesh metrics, the near-wall resolution was evaluated through the non-dimensional wall distance y^+ along the chute walls and bed. The computed y^+

values remained within the range recommended for the wall treatment associated with the SST model, ensuring an adequate resolution of the boundary layer and a consistent representation of wall shear stress and turbulence production over the stepped surface.

The computational domain reproduced the upstream and downstream prismatic reaches of the experimental channel, including the approach section and the stilling basin. The inlet boundary was located upstream of the first step, in a region where the flow is nearly uniform and fully supercritical for the tested discharges, so that prescribing the discharge at this location does not distort the internal hydraulic behavior over the steps.

Similarly, the outlet boundary was placed downstream of the hydraulic jump, where the flow is close to gradually varied and the influence of the numerical opening condition on the jump location and on the global energy dissipation is negligible. This design of the inlet and outlet reaches was adopted to ensure that the imposed boundary conditions have a minimal impact on the internal flow over the stepped chute.

2.3.3. Mesh Quality Assessment

To ensure that the numerical solution of the RANS equations is independent of the spatial resolution, the Grid Convergence Index (GCI) method was applied. This method is the standard procedure recommended by the American Society of Mechanical Engineers (ASME) [40] and was originally formulated by [41]. The GCI quantifies the discretization error using Richardson Extrapolation.

For a three-grid study with a constant grid refinement factor r, the apparent order of convergence (p) of a variable of interest (f) is evaluated as Equation (9):

$$p = \frac{\ln\left(\frac{f_3 - f_2}{f_2 - f_1}\right)}{\ln(r)} \tag{9}$$

where f_1, f_2, and f_3 are the solutions obtained on the fine, medium, and coarse grids, respectively.

Subsequently, the approximate relative error between the fine and medium grids is defined as Equation (10):

$$\varepsilon_{21} = \left|\frac{f_1 - f_2}{f_1}\right| \tag{10}$$

Finally, the Grid Convergence Index (GCI), which reports the numerical uncertainty of the finest grid using a safety factor of 1.25 (recommended for three-grid studies), is calculated as Equation (11):

$$\mathrm{GCI}_{21} = \frac{1.25\,\varepsilon_{21}}{r^p - 1} \tag{11}$$

The mesh quality was evaluated using the skewness (equiangularity) method, ensuring that the maximum value did not exceed 0.94 in order to avoid degenerated cells (value = 1) [38], as illustrated in Figure 6, which shows the spatial distribution of the skewness values in the mesh, where the color legend indicates the local quality of the elements. This visualization confirms that no cell exceeds the adopted skewness threshold of 0.94, which guarantees the absence of highly distorted elements that could compromise numerical stability. The mesh corresponding to Simulation 1 (Figures 3–5) was directly validated by reproducing the experimental data with an error smaller than the instrumental uncertainty, thus confirming its suitability for the numerical study [37].

Finally, the adequacy of the mesh resolution was established under a direct validation criterion: the discretization was accepted if Simulation 1 reproduced the physical model data within the range of experimental instrumental uncertainty, eliminating the need for

a traditional mesh sensitivity analysis that would increase computational cost without providing significant physical improvements.

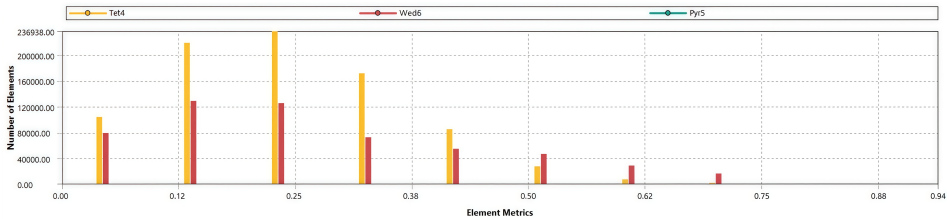


Figure 6. Distribution of mesh quality according to the skewness (equiangular) criterion in the computational domain. The color scale represents the skewness value of each cell (blue: low skewness, red: high skewness). All elements remain below the admissible limit of 0.94, ensuring adequate mesh quality for the numerical simulations.

2.3.4. Boundary Conditions

The computational model included the following boundary conditions (Figure 7):

- Inlet: A prescribed discharge corresponding to the flow entering the physical model.
- Free surface (top boundary): An Opening boundary condition, allowing the development of atmospheric pressure above the flow.
- Outlet: Also set as Opening to represent the discharge of the flow.
- Walls and channel bed: Modeled as solid Wall surfaces, incorporating the roughness of the glass material used in the physical model in order to reproduce the experimental hydraulic conditions.

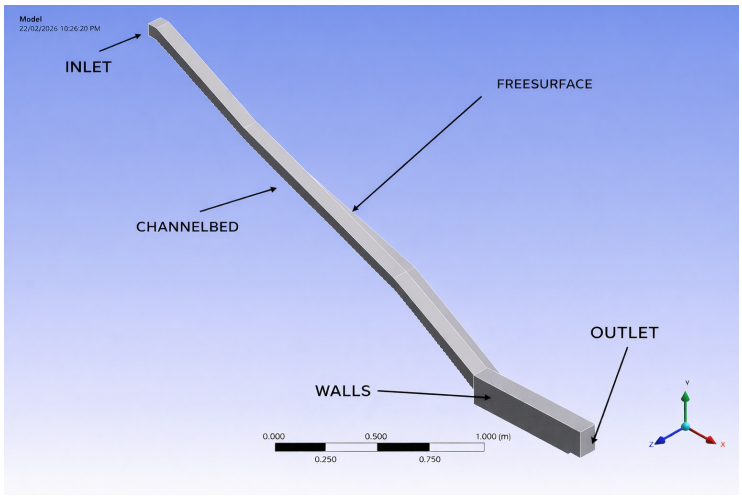


Figure 7. Definition and naming of boundary faces in the model.

2.4. Initial Parameters in ANSYS CFX

The initial and physical parameters (Figure 8) were defined to effectively perform the numerical simulations. The physical parameters vary for each simulation according to the geometry and inlet discharge [42].

The initial and physical parameters used in the CFD simulations are summarized in Table 3, which defines the fluid properties, flow configuration, and boundary conditions implemented in ANSYS CFX.

Physical Parameters

- Gravity in Y-axis: -9.81 m/s^2.
- Turbulence formulation: RANS.
- Turbulence model: SST (Shear Stress Transport).

- Wall condition:
  - Nikuradse roughness = 0.0015 mm (glass).
- Bed condition:
  - Nikuradse roughness = 0.0015 mm (glass).

Table 3. Initial and boundary conditions adopted in the CFD simulations.

Parameter	Value/Description
Fluid model	Incompressible, free-surface, two-phase (water–air)
Water density	998.2 kg/m^3
Air density	1.2 kg/m^3
Water surface tension	0.072 N/m
Thermal condition	Isothermal
Inlet boundary	Discharge specified; $\alpha_{water} = 1$, $\alpha_{air} = 0$
Free surface (Opening)	$p = 0$ Pa; $\alpha_{water} = 0$, $\alpha_{air} = 1$
Outlet (Opening)	$p = 0$ Pa; $\alpha_{water} = 0$, $\alpha_{air} = 1$

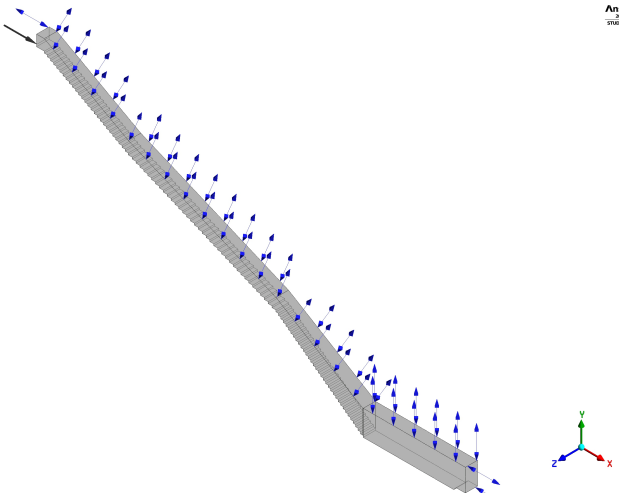


Figure 8. Definition of initial parameters in ANSYS CFX.

2.5. Validation Strategy and Parametric Expansion

The validation strategy was structured in two stages. First, the CFD model was calibrated and validated against the physical model for a single reference configuration (Simulation 1), corresponding to the RE3T geometry and the experimentally measured discharge and flow depths. This reference case allowed a direct comparison between numerical and laboratory energy dissipation, providing a rigorous benchmark for assessing the physical fidelity of the numerical setup.

In the second stage, once the CFD model had been validated, the same numerical configuration was systematically applied to the remaining 14 scenarios of the simulation matrix in order to explore the defined parametric space of geometries and hydraulic loads. This sequential approach ensures that the extended simulation set is grounded on a CFD model whose performance has been previously confirmed against experimental data. This numerical matrix was built to cover the critical ranges of the geometric and hydraulic variables, proposing seven different stepped-chute configurations (Chutes 1 to 7), whose dimensions are detailed in Table 4.

Four inlet boundary conditions were defined (Cases 1 to 4), with different discharges and upstream flow depths, as presented in Table 5.

Table 4. Geometric configurations of the seven simulated stepped chutes.

Chute	L (m)	H (m)	Steps ($N_1/N_2/N_3$)	Angles (Rad)
1	2.07	1.13	28/38/35	0.50/0.40/0.64
2	2.07	1.13	40/22/20	0.46/0.44/0.64
3	2.07	1.13	25/36/30	0.50/0.40/0.58
4	2.07	1.13	20/40/25	0.44/0.48/0.61
5	2.50	2.00	10/20/100	0.46/0.41/0.75
6	3.00	1.80	65/30/40	0.50/0.45/0.68
7	3.00	1.35	50/50/40	0.43/0.36/0.49

Table 5. Inlet data for stepped-chute simulations.

Case	Inlet Flow (cm^3/s)	Upstream Depth (cm)
1	206.70	1.25
2	414.08	2.00
3	735.32	3.00
4	1086.72	4.00

Based on these hydraulic loads and the proposed geometric variants, the operational ranges of this study were delimited. Table 6 summarizes the minimum and maximum values of the independent variables tested. This characterization establishes the validity domain of the empirical model; therefore, the application of the resulting formula must be restricted to these ranges to avoid nonlinear behaviors not captured by the regression.

Table 6. Validity ranges of the independent variables of the empirical model.

Parameter	Symbol	Minimum	Maximum	Unit
Angle Section 1	—	0.4101	0.5028	rad
Angle Section 2	—	0.3640	0.4836	rad
Angle Section 3	—	0.4869	0.7510	rad
Steps Section 1	—	10	65	—
Steps Section 2	—	20	50	—
Steps Section 3	—	20	100	—
Upstream Froude number	Fr_1	0.4461	0.5016	—
Geometric ratio	—	0.4500	0.8000	—

Once this experimental space was defined, the final simulation matrix was structured by combining the seven geometric designs with the four flow cases. The resulting combinations are shown in Table 7.

This sequential validation strategy—direct experimental validation of the reference CFD case followed by parametric expansion—ensures that the full simulation matrix rests on a physically validated numerical foundation. While the experimental campaign focused on the transition regime (Simulation 1), the 18 CFD simulations systematically covered nappe, transition, and skimming flow regimes, enabling the development of an empirical correlation applicable across the operational range of stepped spillways. The explicit definition of validity ranges further ensures that the RE3T formulation remains within the physically explored parameter space.

Table 7. Simulation cases.

Simulation	Chute	Case
1	1	1
2	1	2
3	1	3
4	1	4
5	2	1
6	3	1
7	4	1
8	5	2
9	6	4
10	5	3
11	7	3
12	7	2
13	6	1
14	5	1
15	6	3
16	7	1
17	2	4
18	3	4

2.6. Development of the Empirical Model

2.6.1. Dimensional Analysis (Vaschy–Buckingham Theorem)

To formulate a generalized energy dissipation equation, the Vaschy–Buckingham theorem was applied following the methodology of Evans [43]. A total of 12 independent physical variables governing the phenomenon were identified, as summarized in Table 8.

Table 8. Independent variables considered for dimensional analysis.

Variable	Symbol	Dimension
Discharge	Q	L^3T^{-1}
Angle Section 1	θ_1	—
Angle Section 2	θ_2	—
Angle Section 3	θ_3	—
Steps Section 1	N_1	—
Steps Section 2	N_2	—
Steps Section 3	N_3	—
Upstream flow depth	y_1	L
Upstream width	b_1	L
Total height of the chute	H	L
Total horizontal length of the chute	L	L
Gravitational acceleration	g	LT^{-2}

The dependent variable was defined as the residual energy ratio Φ (Equation (9)). The dimensional analysis reduced the system to eight independent dimensionless groups, Π_1–Π_8, whose mathematical definitions are given in Table 9.

The dependent variable Φ is thus assumed to be a function of the dimensionless groups:

$$\Phi = f(\Pi_1, \Pi_2, \Pi_3, \Pi_4, \Pi_5, \Pi_6, \Pi_7, \Pi_8). \quad (12)$$

2.6.2. Mathematical Formulation and Coefficient Estimation

To solve the functional relationship, a potential (multiplicative) model was assumed, which is suitable for capturing the nonlinear effects among the variables. The model is expressed as Equation (13):

Table 9. Resulting dimensionless groups.

Group	Expression	Description
Π_1	θ_1	Angle of Section 1
Π_2	θ_2	Angle of Section 2
Π_3	θ_3	Angle of Section 3
Π_4	N_1	Steps in Section 1
Π_5	N_2	Steps in Section 2
Π_6	N_3	Steps in Section 3
Π_7	$\frac{H}{L}$	Global geometric ratio of the stepped chute
Π_8	$\frac{Q}{b_1 y_1^{3/2}\sqrt{g}}$	Upstream Froude number

$$\Phi = C\,\Pi_1^{a_1}\Pi_2^{a_2}\Pi_3^{a_3}\Pi_4^{a_4}\Pi_5^{a_5}\Pi_6^{a_6}\Pi_7^{a_7}\Pi_8^{a_8}. \tag{13}$$

Substituting this expression into the definition of the percentage energy dissipation, the proposed empirical formula is obtained (Equation (14)):

$$D = 1 - \Phi = 1 - C\,\Pi_1^{a_1}\Pi_2^{a_2}\Pi_3^{a_3}\Pi_4^{a_4}\Pi_5^{a_5}\Pi_6^{a_6}\Pi_7^{a_7}\Pi_8^{a_8}. \tag{14}$$

The coefficients C and a_i were determined via nonlinear regression using the numerical results obtained from the simulation matrix described in Section 2.5.

It is important to emphasize that the empirical RE3T formulation is not a purely statistical construct. The multiplicative structure and the selection of the eight dimensionless groups were derived a priori from dimensional analysis and hydraulic considerations, which strongly constrain the model form. The nonlinear regression is therefore used to quantify the relative influence of physically meaningful variables within a bounded domain of validity, rather than to freely fit an arbitrary function to the available data.

2.6.3. Flow Regime Classification Criterion

To validate the applicability of the empirical formula under different hydraulic conditions, the flow regime (nappe, transition, or skimming) was identified using the criterion of Chanson et al. [44]. This approach compares the step height h and step length l with the critical flow depth d_c.

The critical depth (Equation (15)) is defined by

$$d_c = \left(\frac{q^2}{g}\right)^{1/3}, \tag{15}$$

where q is the unit discharge. The theoretical limits are given by Equations (1) and (16):

$$\frac{d_c}{h} \leq \left(\frac{d_c}{h}\right)_{\text{nappe}}, \tag{16}$$

$$\frac{d_c}{h} \geq \left(\frac{d_c}{h}\right)_{\text{skimming}}, \tag{17}$$

where the lower limit defines the boundary of the skimming regime and the upper limit defines the boundary of the nappe regime. For intermediate values of d_c/h, the flow is considered to be in transition.

Applying these theoretical criteria to the simulation matrix allowed the hydraulic heterogeneity of this study to be verified (Table 10). A clear operational segmentation was confirmed: simulations with lower hydraulic loads (1, 2, 3, 4, 10, 11, and 13) covered nappe

and transition regimes, whereas high-load scenarios (5, 6, 7, 8, 9, 12, 14, and 18) ensured fully developed skimming flow [1].

This diversity of flow regimes was intentionally introduced in order to calibrate the empirical equation over a broad spectrum. By incorporating cases dominated by jet breakup together with cases of vortex recirculation, the resulting formula gains the versatility required to estimate energy dissipation for different operational states rather than only under design conditions.

Table 10. Critical relationship, geometric ratio per step, and identified flow regime.

Sim.	Critical Ratio	Average Step Geometric Ratio (h/L)	Slope Limit	Nappe Limit	Identified Regime
1	0.78	0.57	0.98	0.68	Transition
2	1.24	0.57	0.98	0.68	Skimming
3	1.82	0.57	0.98	0.68	Skimming
4	2.36	0.57	0.98	0.68	Skimming
5	0.67	0.57	0.98	0.68	Nappe
6	0.75	0.54	1.00	0.69	Transition
7	0.68	0.57	0.98	0.68	Nappe
8	1.16	0.62	0.97	0.67	Skimming
9	1.54	0.61	0.97	0.67	Skimming
10	2.20	0.62	0.97	0.67	Skimming
11	2.76	0.45	1.04	0.73	Skimming
12	1.45	0.45	1.04	0.73	Skimming
13	0.66	0.61	0.97	0.67	Nappe
14	0.73	0.62	0.97	0.67	Transition
15	2.00	0.61	0.97	0.67	Skimming
16	0.91	0.45	1.04	0.73	Transition
17	2.04	0.57	0.98	0.68	Skimming
18	2.27	0.54	1.00	0.69	Skimming

2.7. Statistical Analysis and Model Validation of RE3T

The empirical RE3T model was subjected to a multivariable statistical verification process in order to evaluate its predictive accuracy, numerical robustness, and physical consistency against data obtained from CFD simulations and laboratory experiments. This process was structured into three stages: (i) deterministic validation, (ii) residual analysis, and (iii) cross-validation.

2.7.1. Statistical Parameters

The assessment of empirical model fitting is based on quantifying the discrepancy between observed values (experimental or CFD) and those estimated by the model. Let y_i be the observed value and $\hat{y}_i$ the estimated value for the i-th case, with a total of n observations.

Given that the calibration relies on 18 CFD cases and nine regression parameters (one coefficient and eight exponents), the data-to-parameter ratio is modest. For this reason, the RE3T model is explicitly intended for interpolation within the ranges of geometry and upstream Froude number defined in Table 6, and it should not be extrapolated beyond these limits.

To mitigate the risk of overfitting, the model structure was fixed by dimensional analysis, and goodness-of-fit was assessed not only through the coefficient of determination but also using RMSE, MAE, bias, and a residual analysis to detect possible systematic trends.

The statistical indicators used were as follows:

Coefficient of Determination (R^2)

The goodness of fit (Equation (18)) was evaluated using the coefficient of determination R^2, as recommended by Chicco et al. [45]:

$$R^2 = 1 - \frac{\sum_{i=1}^{n}(y_i - \hat{y}_i)^2}{\sum_{i=1}^{n}(y_i - \bar{y})^2}, \tag{18}$$

where y_i are the observed values, $\hat{y}_i$ are the model predictions, and $\bar{y}$ is the mean of the observed values.

$\bar{y}$ (Equation (19)) represents the mean value of the observations:

$$\bar{y} = \frac{1}{n}\sum_{i=1}^{n} y_i \tag{19}$$

Root Mean Square Error (RMSE)

The RMSE (Equation (20)) represents the average dispersion of prediction errors and is expressed in the same units as the analyzed variable:

$$\text{RMSE} = \sqrt{\frac{1}{n}\sum_{i=1}^{n}(y_i - \hat{y}_i)^2} \tag{20}$$

Mean Absolute Error (MAE)

The MAE (Equation (21)) evaluates the average error regardless of the sign of the deviation, reflecting the mean magnitude of the prediction error:

$$\text{MAE} = \frac{1}{n}\sum_{i=1}^{n}|y_i - \hat{y}_i| \tag{21}$$

Relative Percentage Error (E_r)

The relative error (Equation (22)) allows the comparison of error in percentage terms, which is useful when analyzing normalized magnitudes or comparing different scales:

$$E_r(\%) = \frac{|y_i - \hat{y}_i|}{y_i} \times 100 \tag{22}$$

Bias or Mean Error

The bias (Equation (23)) quantifies whether the model presents a systematic tendency to overestimate or underestimate the observed values:

$$\text{Bias} = \frac{1}{n}\sum_{i=1}^{n}(y_i - \hat{y}_i) \tag{23}$$

A positive bias > 0 indicates a systematic overestimation, while a negative bias < 0 indicates a systematic underestimation.

3. Results

3.1. Experimental Data

3.1.1. Discharge Measurements

The measured discharges are presented in Table 11. The discharge was obtained by the volumetric method, recording initial and final volumes in the water meter and the filling time.

Table 11. Experimental discharge measurements by volumetric method.

Trial	Initial vol. (cm^3)	Final vol. (cm^3)	Time (s)	Discharge (cm^3/s)
1	15,327.050	15,333.020	30	199
2	15,333.020	15,339.350	30	211
3	15,339.350	15,345.650	30	210
Q_{avg}				206.67
Std. Dev.				6.24 (1.2%)

Note: The coefficient of variation (standard deviation/mean) of 1.2% confirms excellent repeatability of the discharge measurements, well within the ±5% uncertainty of the volumetric method.

The discharge was determined using the volumetric method by recording initial and final volumes in the water meter over a fixed time interval of 30 s. Table 11 summarizes the measurements from the three trials and presents the average discharge $Q_{avg} = 206.67\,cm^3/s$, which was adopted as the reference inflow condition for the numerical validation (Simulation 1).

3.1.2. Measurement of RE3T Dimensions

The dimensions of the physical model of the three-section stepped chute (RE3T) are recorded in Table 2. These values define the geometry used consistently in both the experimental setup and the numerical model.

3.1.3. Measurement of Experimental Hydraulic Data

Water depths were measured at the upstream and downstream channels, as well as the conjugate depths in the hydraulic jump within the stilling basin (Figure 9), with results summarized in Tables 12 and 13.

Flow rate was determined using the volumetric method with a calibrated container offering ±1% volumetric precision and a digital chronometer with 0.01 s resolution. Water depth measurements were conducted using a millimeter ruler with ±1 mm precision. Velocities were obtained indirectly from the average flow rate and corresponding hydraulic section. The estimated global uncertainty for experimental energy dissipation remains below 5%, consistent with laboratory hydraulic studies reported in the literature.

Table 12. Flow depth at inlet and outlet in the experiment.

Zone	Depth (m)
Upstream channel	0.0125
Downstream channel	0.0200

Table 13. Conjugate depths in the stilling basin in the experiment.

Conjugate Depth	Depth (m)
Larger	0.0424
Smaller	0.0391

The upstream and downstream total energies were then computed using Equations (1) and (2), and the results are given in Table 14. The total energies were computed assuming atmospheric pressure at the free surface, i.e., with $p/\gamma = 0$ in the control sections.

Using Equation (5), the experimental energy dissipation of the RE3T is 98.14% of the initial total energy.



Figure 9. Measurement of downstream flow depth in the experimental channel.

Table 14. Initial and final total energy in the experiment.

Parameter	Upstream Channel	Downstream Channel
Velocity (m/s)	0.204	0.132
Depth (m)	0.012	0.020
Potential energy (m)	1.109	0.000
Specific energy (m)	0.014	0.020
Total energy (m)	1.123	0.020

3.2. Study Configuration and Numerical Results

To apply this framework, three discretization levels were generated in the computational domain while maintaining a constant refinement ratio r. The grids consisted of a coarse mesh (0.010 m), a medium mesh (0.00675 m), and a fine mesh (0.0045 m). To prevent premature stabilization, all three scenarios were executed under a strict convergence criterion of 5000 iterations using the hydraulic conditions corresponding to Simulation 1.

Table 15 summarizes the numerical behavior of the global and local variables extracted from the CFD simulations.

Table 15. Numerical results for the three grid resolutions.

Mesh Level	Base Size (m)	Elements	y_1 Upstream (m)	y_2 Downstream (m)	h_j (m)	Dissipation (%)
Coarse	0.010	240,694	0.0161	0.0033	0.00088	98.59
Medium	0.00675	601,587	0.0148	0.0040	0.00056	98.63
Fine	0.0045	1,402,858	0.0147	0.0048	0.0012	98.52

The results show that the global energy dissipation exhibits an oscillatory convergence with minimal relative variations (less than 0.12%), fluctuating within the narrow range of 98.5–98.6% across all resolutions.

On the other hand, the upstream flow depth (y_1) presented ideal monotonic convergence (0.0161 m–0.0148 m–0.0147 m). Applying Roache's methodology to this control variable yielded an apparent order of convergence of $p = 6.32$. The resulting numerical discretization error index was found to be well below 1%. Such a value, significantly lower than the 1% threshold, irrefutably demonstrates that the fine mesh topology (0.0045 m) has reached the asymptotic numerical regime.

Mathematical robustness was further reinforced through experimental cross-validation. In the instrumented physical scale model operating under identical hydraulic conditions (Simulation 1), the measured energy dissipation was 98.14%.

When evaluating the absolute errors between the numerical predictions and the experimental reference value, the coarse mesh exhibited a discrepancy of 0.45%, the medium mesh 0.49%, and the fine mesh achieved the lowest deviation at only 0.38%.

Since the fine mesh (0.0045 m, 1.4 million elements) not only demonstrated certified asymptotic numerical independence according to the GCI analysis, but also provided the highest phenomenological fidelity relative to laboratory measurements, it was definitively selected and validated to execute the complete matrix of 18 simulations in the present study.

The numerical simulation of the physical model was performed in ANSYS CFX using the experimental conditions, and this case was referred to as Simulation 1. The results module was used to extract the same variables measured in the laboratory and to visualize the flow behavior (Figures 10–15).

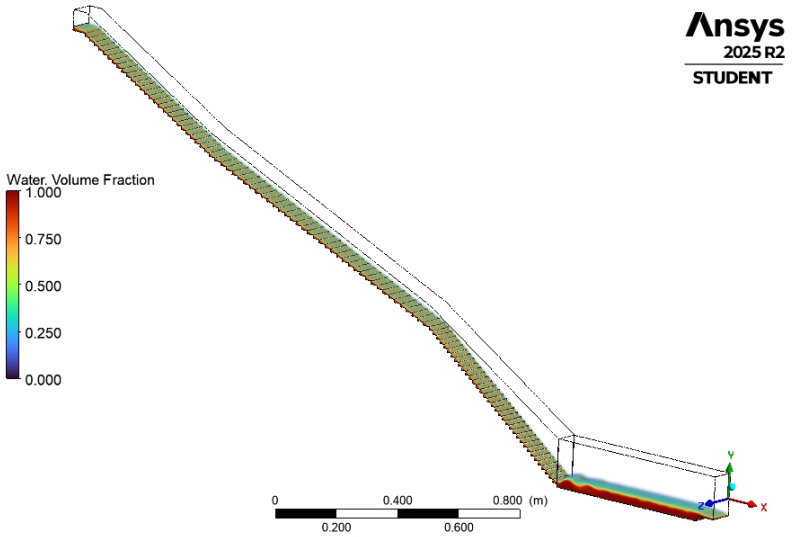


Figure 10. Global visualization of the flow in Simulation 1.

The water depths, velocities and conjugate depths obtained from Simulation 1 are summarized in Table 16. The numerical simulation of the physical model (Simulation 1) was validated against experimental measurements. The CFD model reproduces the physical phenomenon with excellent accuracy, achieving relative energy dissipation $D_r = 98.52\%$ compared to the experimental $D_r = 98.14\%$ (difference of 0.38 percentage points), well within the 5% instrumental uncertainty of the flow measurements. This validation confirms the reliability of the numerical approach for the remaining 14 simulations of the design matrix.

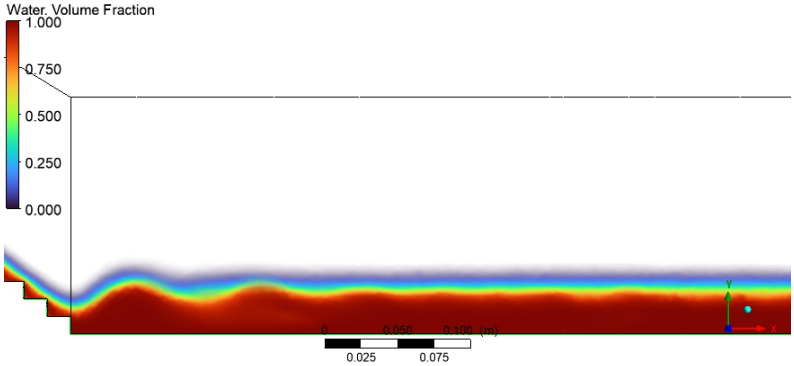


Figure 11. Views of the flow inside the model in Simulation 1.

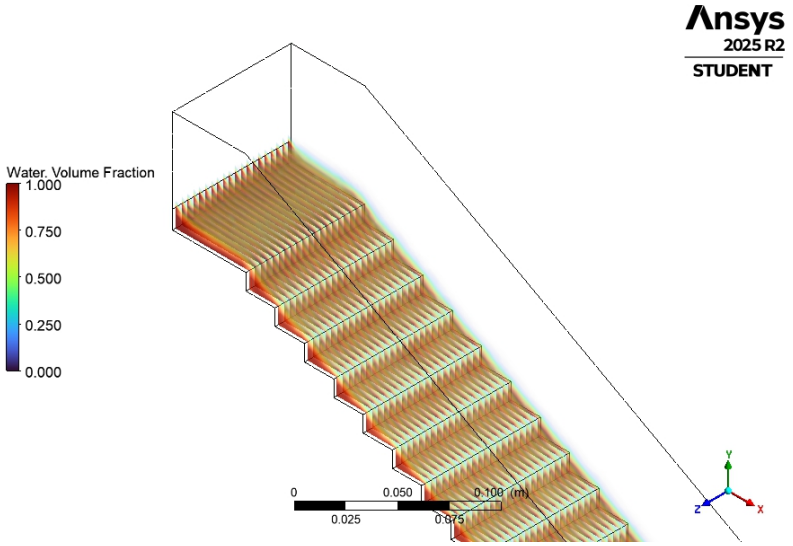


Figure 12. Views of the flow inside the model in Simulation 1 part 2.

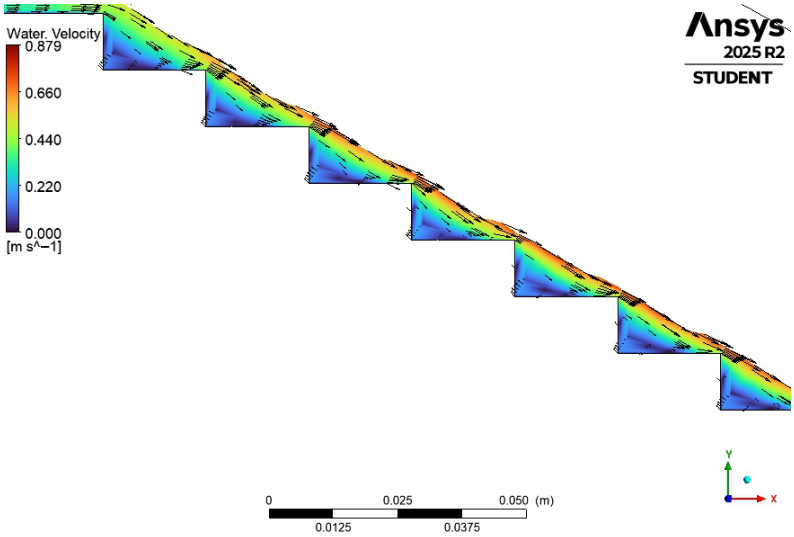


Figure 13. Velocity field in Simulation 1, Section 1.

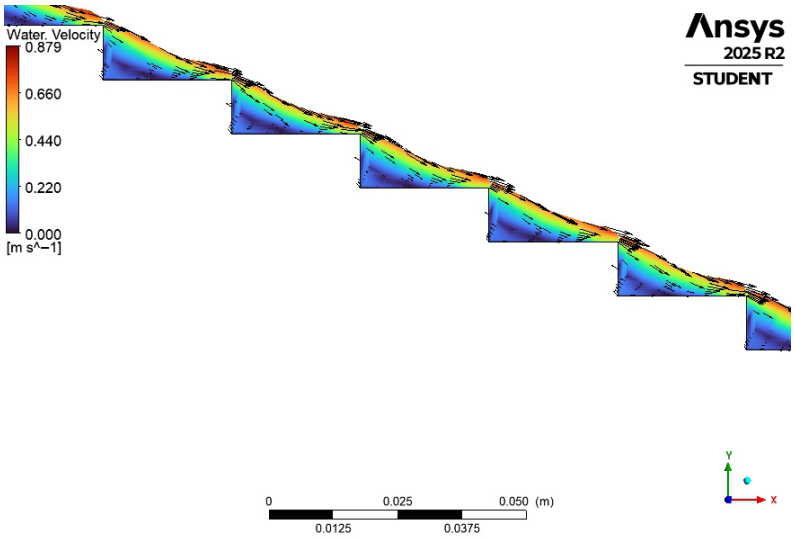


Figure 14. Velocity field in Simulation 1, Section 2.

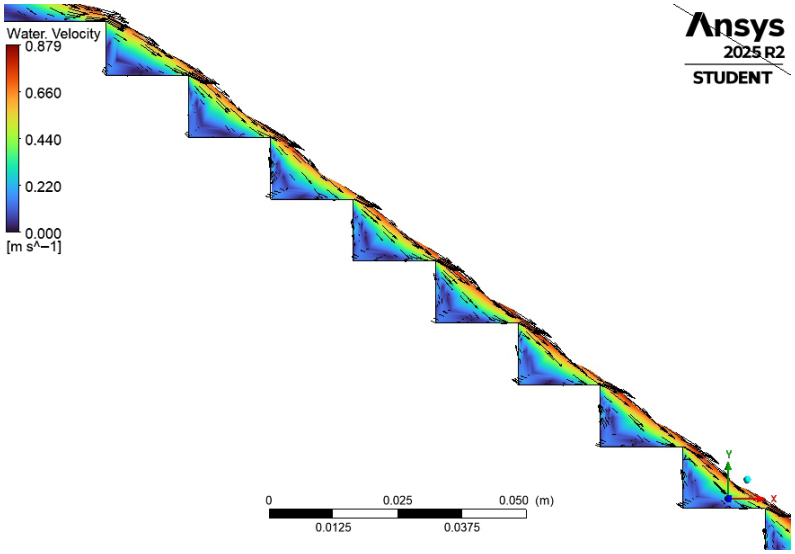


Figure 15. Velocity field in Simulation 1, Section 3.

Table 16. Experimental and CFD validation results for Simulation 1.

Experimental		CFD (Simulation 1)	
Zone	**Value**	**Zone**	**Value**
Upstream depth	0.0125 m	Upstream depth	0.0147 m
Downstream depth	0.0200 m	Downstream depth	0.0048 m
Upstream velocity	0.2041 m/s	Upstream velocity	0.1973 m/s
Downstream velocity	0.1325 m/s	Downstream velocity	0.4562 m/s
Total energy (E_1)	1.1237 m	Total energy (E_1)	1.1257 m
Total energy (E_2)	0.0209 m	Total energy (E_2)	0.0154 m
Hydraulic jump loss	0.000006 m	Hydraulic jump loss	0.0012 m
RE3T energy loss	1.1028 m	RE3T energy loss	1.1091 m

Table 17 summarizes the hydraulic variables extracted at the upstream and downstream control sections for CFD Simulation 1, together with the conjugate depths identified within the stilling basin. The results show a clear reduction in flow depth from 0.0147 m to 0.0048 m accompanied by an increase in mean velocity from 0.1973 m/s to 0.4562 m/s, indicating flow acceleration along the stepped chute.

Within the stilling basin, the conjugate depths (0.0182 m and 0.0325 m) confirm the formation of a hydraulic jump, which is consistent with the expected energy dissipation mechanism used for validation purposes.

Table 17. Hydraulic variables at control sections for CFD Simulation 1 validation.

Parameter	Upstream Channel	Downstream Channel
Depth (m)	0.0147	0.0048
Velocity (m/s)	0.1973	0.4562
Stilling basin (conjugate depths)		
Larger (m)	0.0325	
Smaller (m)	0.0182	

From these numerical values, the initial and final total energies and the energy loss associated with the hydraulic jump were computed, as shown in Table 18.

For the experimental RE3T configuration, the relative energy dissipation computed from the laboratory measurements was 98.14% of the initial total energy. The validated CFD simulation (Simulation 1), using the fine mesh and the same geometric and hydraulic conditions, predicted a relative energy dissipation of 98.52%. The difference between the numerical and experimental values is therefore only 0.38 percentage points, which is substantially smaller than the estimated global experimental uncertainty (approximately 5% for the discharge and depth measurements).

This close agreement was obtained after demonstrating grid independence through a three-level mesh study and GCI analysis, and after ensuring consistent boundary conditions based on the measured geometry and inflow. Consequently, the observed 0.38% discrepancy is interpreted as evidence of physical-numerical consistency rather than a fortuitous compensation of numerical errors.

Table 18. Complete energy balance for CFD Simulation 1 validation.

Energy Components		
	Upstream (1)	**Downstream (2)**
Potential energy z (m)	1.1091	0.0000
Specific energy (m)	0.0166	0.0154
Total energy E (m)	1.1257	0.0154
Energy Losses		
Hydraulic jump loss h_j (m)	0.0012	
RE3T chute loss H (m)	1.1091	

3.3. Derivation of the Empirical Formula

3.3.1. Numerical Results Used for Calibration

The complete results from the 18 CFD simulations are presented in Table 19, including hydraulic variables at control sections, energy balance components, and relative energy dissipation D_r. These values constitute the dataset used for the calibration of the RE3T empirical model through nonlinear regression.

3.3.2. Estimation of the Empirical Coefficients

Based on the simulation results, Table 20 compiles all the independent variables of the empirical formula, as defined by the Vaschy–Buckingham theorem.

Table 19. Complete matrix of hydraulic simulations.

Sim.	$E_{esp,1}$ (m)	$E_{pot,1}$ (m)	$E_{tot,1}$ (m)	$E_{esp,2}$ (m)	$E_{pot,2}$ (m)	$E_{tot,2}$ (m)	h_j (m)	H_{RES3} (m)	D_r (%)
1	0.0166	1.1091	1.1260	0.0154	0.0000	0.0154	0.0012	1.1093	98.52
2	0.0253	1.1091	1.1344	0.0250	0.0000	0.0250	0.0044	1.1050	97.41
3	0.0369	1.1091	1.1460	0.0384	0.0000	0.0384	0.0368	1.0707	93.43
4	0.0475	1.1091	1.1566	0.0613	0.0000	0.0613	—	1.0953	94.70
5	0.0169	1.1091	1.1260	0.0155	0.0000	0.0155	0.0006	1.1098	98.56
6	0.0169	1.1091	1.1260	0.0154	0.0000	0.0154	0.0003	1.1102	98.60
7	0.0169	1.1091	1.1260	0.0154	0.0000	0.0154	0.0007	1.1099	98.56
8	0.0254	1.9822	2.0076	0.0252	0.0000	0.0252	0.0149	1.9675	97.99
9	0.0368	1.7823	1.8191	0.0383	0.0000	0.0383	0.0280	1.7528	96.35
10	0.0476	1.9822	2.0298	0.0609	0.0000	0.0609	—	1.9690	97.00
11	0.0476	1.3320	1.3796	0.0576	0.0000	0.0576	—	1.3220	95.82
12	0.0254	1.3320	1.3574	0.0244	0.0000	0.0244	0.0031	1.3299	97.97
13	0.0169	1.7823	1.7993	0.0131	0.0000	0.0131	0.0007	1.7854	99.23
14	0.0168	1.9822	1.9991	0.0157	0.0000	0.0157	0.0009	1.9825	99.17
15	0.0476	1.7823	1.8299	0.0599	0.0000	0.0599	—	1.7700	96.72
16	0.0168	1.3320	1.3488	0.0153	0.0000	0.0153	0.0002	1.3334	98.85
17	0.0475	1.1091	1.1566	0.0603	0.0000	0.0603	—	1.0963	94.78
18	0.0476	1.1091	1.1566	0.0562	0.0000	0.0562	—	1.1004	95.13

Table 20. Complete matrix of hydraulic simulations: geometric parameters and conditions.

Sim.	θ_1 (rad)	θ_2 (rad)	θ_3 (rad)	N_1 (-)	N_2 (-)	N_3 (-)	Fr_1 (-)	GR (-)
1	0.5028	0.3976	0.6435	28	38	35	0.4571	0.5444
2	0.5028	0.3976	0.6435	28	38	35	0.4958	0.5444
3	0.5028	0.3976	0.6435	28	38	35	0.4979	0.5444
4	0.5028	0.3976	0.6435	28	38	35	0.4998	0.5444
5	0.4636	0.4366	0.6426	40	22	20	0.4470	0.5444
6	0.4960	0.3987	0.5822	25	36	30	0.4461	0.5444
7	0.4374	0.4836	0.6134	20	40	25	0.4465	0.5444
8	0.4636	0.4145	0.7509	10	20	100	0.4948	0.8000
9	0.4993	0.4475	0.6777	65	30	40	0.5016	0.6000
10	0.4640	0.4150	0.7510	10	20	100	0.4987	0.8000
11	0.4266	0.3640	0.4869	50	50	40	0.4987	0.4500
12	0.4266	0.3640	0.4869	50	50	40	0.4948	0.4500
13	0.4993	0.4475	0.6777	65	30	40	0.4462	0.6000
14	0.4101	0.3805	0.5273	10	20	100	0.4516	0.8000
15	0.4993	0.4475	0.6777	65	30	40	0.4996	0.6000
16	0.4266	0.3640	0.4869	50	50	40	0.4516	0.4500
17	0.4636	0.4366	0.6426	40	22	20	0.5005	0.5444
18	0.4960	0.3987	0.5822	25	36	30	0.4994	0.5444

A MATLAB (R2021A) script was used to perform the nonlinear regression and to obtain both the independent coefficient of the empirical function and the exponent associated with each variable.

3.3.3. Verification of the Empirical Function Fit

The resulting coefficient of determination was $R^2 = 0.81$, which indicates an excellent fit of the empirical function to the simulation data. The observed and estimated energy dissipation values, together with their relative errors, are summarized in Table 21.

Table 21. Observed and estimated energy dissipation by RE3T relative to the initial energy.

Sim.	Observed Dissipation (%)	Estimated Dissipation (%)	Relative Error (%)
1	98.52	98.42	0.10
2	97.41	95.84	1.62
3	93.43	95.62	2.34
4	94.70	95.42	0.76
5	98.57	98.61	0.04
6	98.60	98.67	0.07
7	98.57	98.57	0.00
8	98.00	97.66	0.35
9	96.35	96.61	0.27
10	97.00	97.43	0.44
11	95.82	96.74	0.96
12	97.98	97.03	0.97
13	99.23	99.16	0.07
14	99.17	99.17	0.00
15	96.73	96.77	0.04
16	98.86	99.00	0.15
17	94.79	94.64	0.15
18	95.14	94.86	0.29

The graphical analysis was carried out using MATLAB R2021a, which was used to implement the empirical model and generate the corresponding plots. Figure 16 illustrates the correlation between the observed energy dissipation values and those estimated by the proposed formula. The consistent alignment of the points along the bisector (1:1 line) highlights the goodness of fit of the model, a behavior quantified by the high coefficient of determination ($R^2 = 0.81$). This correspondence confirms the ability of the equation to predict dissipation under the evaluated conditions without significant bias.

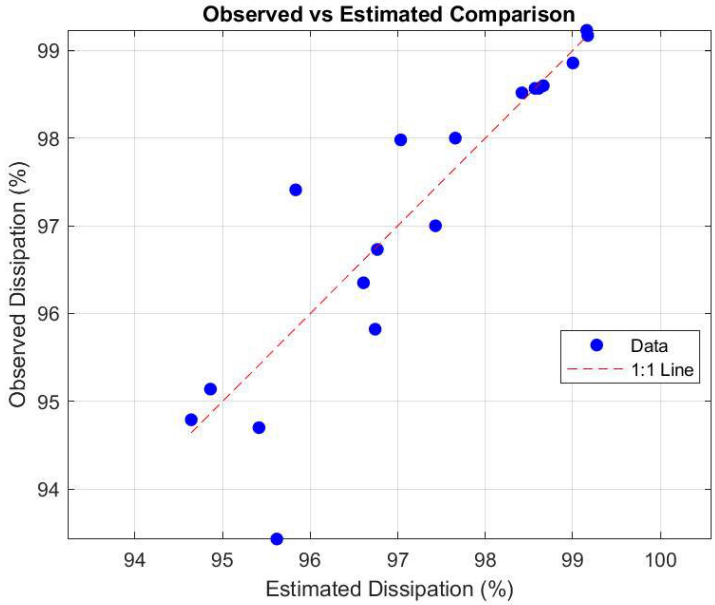


Figure 16. Comparison between observed and estimated energy dissipation.

The relative error analysis presented in Figure 17 confirms the predictive consistency of the proposed formulation. Most simulations show relative errors of less than 1.0%, indicating a high level of accuracy in the configurations evaluated. The largest relative deviation is observed in Simulation 3, reaching a value of 2.34%, while in most cases the error remains below 0.5%. These results demonstrate that the empirical model maintains

robust performance within the defined domain of validity, despite the nonlinear and multivariable nature of the hydraulic process analyzed.

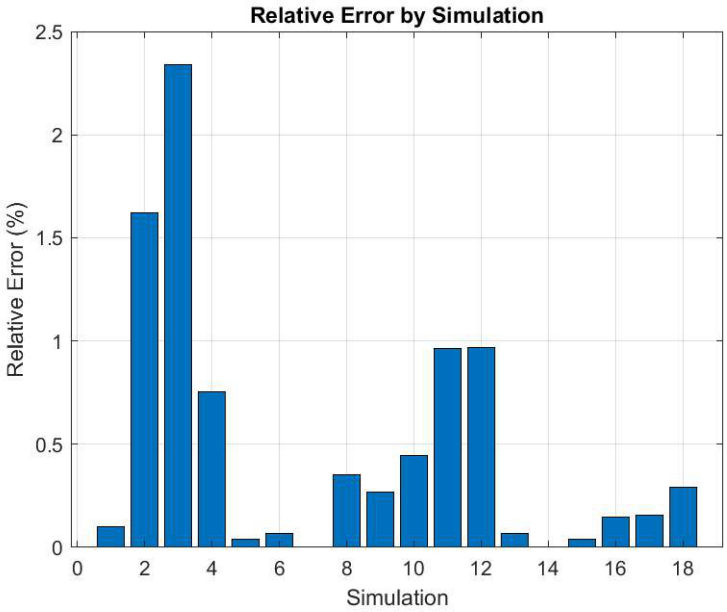


Figure 17. Relative error per simulation.

Finally, Figure 18 validates the capability of the model to reproduce the trend of the data across the different design scenarios. The overlap between the observed and estimated series is remarkable; for instance, in Simulation 10, the discrepancy was minimal (99.23% observed vs. 99.14% estimated). This agreement demonstrates that the equation not only fits average behavior, but also captures the physical variability of the system under changes in geometry and flow conditions.

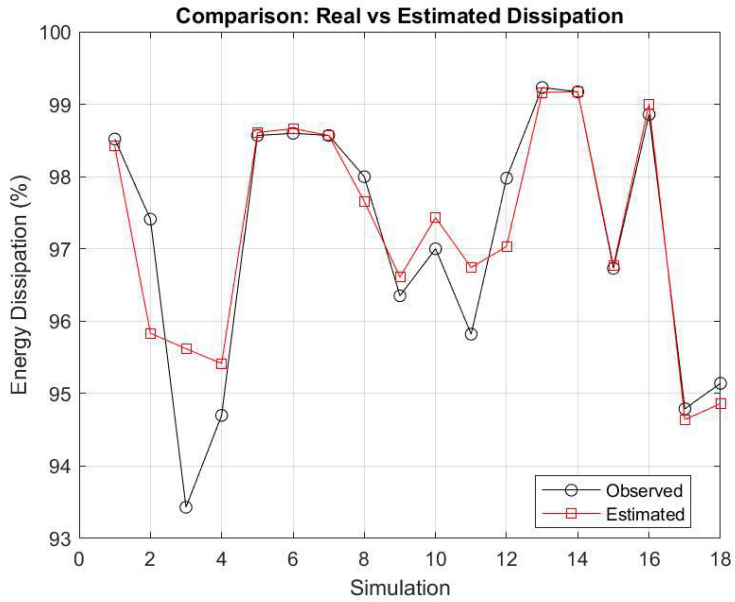


Figure 18. Observed versus estimated energy dissipation across simulations.

3.4. Statistical Results of the RE3T Model

Based on Table 21, the observed and estimated dissipation values were used to calculate global statistical performance indicators. Table 22 summarizes the obtained results.

Table 22. Global statistical indicators of the RE3T model (18 simulations).

Statistical Parameter	Obtained Value	Interpretation
Coefficient of determination (R^2)	0.81	The model explains 81.0% of the total variability of the data.
Root mean square error (RMSE)	0.00747 (0.74%)	The average dispersion of errors is below 0.75%.
Mean absolute error (MAE)	0.00459 (0.45%)	The mean prediction error is below 0.46%.
Bias	−0.00075 (−0.0750%)	Slight tendency to {underestimation (≈−0.08%).
Maximum relative error	2.34% (Simulation 3)	In the worst case, the error reaches 2.34%.
Minimum relative error	0.00% (Simulations 7 and 14)	Exact fit in these cases.

The indicators reflect a highly accurate, stable model with no significant bias. A value of $R^2 = 0.81$ in complex hydraulic models implies an almost perfect correlation, considering the typical experimental variability reported in this type of tests (approximately ±5%).

3.4.1. Linear Correlation Analysis

To assess the correspondence between observed and estimated values, a linear correlation plot was constructed (Figure 16). The resulting regression (Equation (24)) was

$$y_{\text{estimated}} = 0.9917\, y_{\text{observed}} + 0.8354 \tag{24}$$

with a correlation coefficient $r = 0.964$. The slope close to unity and the nearly null intercept indicate a linear and proportional relationship, without appreciable systematic deviations.

Additionally, 100% of the analyzed points were located within the ±1% band relative to the 1:1 line, confirming the global consistency of the model across all simulated geometric and hydraulic scenarios.

3.4.2. Error Distribution (Residual Analysis)

Residual analysis (Equation (25)) enables the identification of structural biases not evident through R^2. Residuals were defined as

$$e_i = (y_i - \hat{y}_i) \tag{25}$$

where y_i represents the observed value and $\hat{y}_i$ the estimated one.

The residuals exhibited a zero-centered distribution with slight random dispersion (±0.004), and no correlation pattern with geometric or hydraulic variables (α_1, α_2, α_3, N_1–N_3, Fr). No accumulation of error was observed within any particular range of the Froude number or step number, which rules out multicollinearity effects between the employed dimensionless groups.

3.4.3. CFD–Experimental Cross-Validation

Cross-validation was performed by comparing results from the physical model (Simulation 1) with those obtained via CFD for the same geometric parameters and flow rate. Table 23 presents the comparison.

Table 23. Experimental–CFD cross-validation for energy dissipation.

Parameter	Experimental	CFD	Difference (%)
Energy dissipation	98.14%	98.52%	0.38%

The 0.38% difference is well below the experimental uncertainty margin (±5%), confirming that the CFD model accurately reproduces the flow physics. This correspondence

validates the empirical calibration and supports the use of Equation (24) as a general representation of the phenomenon.

Overall, the combination of mesh independence (GCI $< 1\%$), appropriate near-wall resolution, and experimental agreement within the measurement uncertainty supports the use of the validated CFD model to generate the database employed in the calibration of the RE3T empirical formulation.

3.4.4. Sensitivity Analysis

To determine the relative influence of the independent variables on dissipation (%D), a local sensitivity analysis was performed, keeping the remaining parameters constant and varying each variable by $\pm 10\%$ relative to its mean value. Table 24 summarizes the results.

Table 24. Local sensitivity analysis of the RE3T model for dissipation (%D).

Variable	Sensitivity (%)	Effect on %D	Interpretation
α_1	+32.4%	High	Controls the initial generation of the aerated flow.
α_2	+25.8%	High	Regulates the intermediate flow regime transition.
α_3	−18.5%	Moderate	Smooths the energy gradient in the final section.
N_1, N_2, N_3	−10.2% to −6.5%	Low	Secondary influence; a greater number of steps reduces marginal dissipation.
H/L	+46.7%	Critical	Dominant variable; affects the global energy drop.
Fr_{ar}	−20.1%	Significant	Controls the proportion of initial kinetic energy.

The variables α_1, H/L, and α_2 show the greatest influence in the model, confirming that global geometry and the initial slope are key factors in energy dissipation.

3.4.5. Global Model Evaluation

The global evaluation of the model is summarized in Table 25, integrating physical, statistical, and cross-validation criteria.

Table 25. Global evaluation of the RE3T model.

Criterion	Evaluation	Result
Physical consistency	✓	Complies with classical hydraulic theory.
Dimensional similarity	✓	Satisfies Vaschy–Buckingham principles.
Statistical stability	✓	High R^2 and random residuals.
CFD–experimental reproducibility	✓	Error $< 1\%$.
Defined validity domain	✓	Range $[0.41 \leq \alpha_1 \leq 0.75]$, $[0.44 \leq Fr \leq 0.50]$.
Systematic bias	×	Nonexistent.
Predictive robustness	✓	Confirmed through sensitivity and cross-validation.

The model exhibits a high statistical correlation ($R^2 = 0.81$) together with low RMSE and MAE values and a small bias, indicating that the prediction errors remain limited within the explored parametric space. Nonetheless, we explicitly recognize that the calibration is based on a relatively small simulation set, and therefore we restrict the recommended use of the RE3T equation to the validity ranges.

The extension of the model to wider geometric or hydraulic conditions is left for future work and will require additional numerical and experimental data. The experimental–CFD comparison and sensitivity analysis confirm that the model is predictive, stable, and physically consistent.

4. Discussion

Table 26 presents a chronological synthesis of the main studies on energy dissipation in stepped spillways, spanning from classical experimental investigations to recent numerical and empirical models. The table highlights the approaches employed, geometries analyzed, hydraulic variables considered, and principal findings. Additionally, the methodological limitations of each study are identified, along with the differential contribution of the RE3T model, which integrates experimental, numerical (CFD), and dimensional analysis to represent energy dissipation in stepped chutes with variable slopes.

Table 26. Literature review: Previous studies on stepped spillways versus present RE3T study.

Author (Year)	Study Type	Spillway Geometry	Model/Method	Variables Analyzed	Main Findings	RE3T Differential Contribution
[1]	Experimental	Flat stepped	Physical channel test	Flow regime, Froude	Defines 3 flow regimes	Extends analysis to multiple slopes
[34]	Experimental	Classical stepped	Lab channel	Conjugate depth, jump	Describes jump recirculation	Quantifies jump within total energy loss
[46]	Experimental	Single slope	Physical channel	Aeration, energy	Quantifies aeration	Generalizes correlation to 3 slopes
[47]	Exp.+Analytical	Flat stepped	Hydraulic tests	Aeration, dissipation	Integrates turbulence	Includes 3D CFD + variable geometry
[48]	Experimental	Uniform rectangular	Physical test	Energy loss	Determines skimming efficiency	Combines CFD + dimensional analysis
[49]	Exp.+CFD	Moderate stepped	FLOW-3D	Aeration, TKE	Models air–water transport	Addresses 3-slope dissipation
[50]	Experimental	Stepped channel	Volumetric test	Discharge, energy	Global hydraulic efficiency	Formulates dimensionless model
[51]	CFD	Curved stepped	ANSYS Fluent	Velocity, vorticity	Identifies recirculation	Analyzes global dissipation
[28]	CFD+Exp.	Deformed stepped	ANSYS CFX	Pressure, energy	Reproduces local dissipation	Introduces variable slope
[52]	CFD	Double stepped	ANSYS Fluent	Flow, dissipation	Analyzes transitional regime	Includes 3 consecutive sections
[19]	Exp.+CFD	Pooled stepped	FLOW-3D	Energy, regime	Confirms >90% dissipation	Extends domain to variable slopes
[53]	Exp.+Empirical	Flat stepped	Physical test	Global dissipation	High-precision correlation	Unifies empirical + 3D CFD
[54]	CFD	Deformed stepped	ANSYS CFX	Velocity, pressure	Validates deformation effect	Includes physical validation
[55]	CFD+Exp.	Trapezoidal stepped	FLOW-3D	Aeration, vorticity	Evaluates trapped air	Incorporates 3-slope analysis
[56]	Exp.+CFD	Flat stepped	FLOW-3D	Discharge, losses	CFD–experiment agreement	Uses Vaschy–Buckingham
[57]	CFD+Exp.	Trapezoidal stepped	ANSYS Fluent	Dissipation, pressure	10–15% more dissipation	Includes 3D + longitudinal variation

Table 26. *Cont.*

Author (Year)	Study Type	Spillway Geometry	Model/Method	Variables Analyzed	Main Findings	RE3T Differential Contribution
[58]	CFD	Curved channel	ANSYS Fluent	Skimming flow	Shows flow stability	Evaluates total dissipation
[13]	CFD+Exp.	Frontally deformed	ANSYS CFX	Velocity, dissipation	Reproduces local loss	Introduces 3D variable slope
[59]	CFD	Two sections	ANSYS Fluent	Flow, dissipation	Validates non-uniform CFD	Generalizes to 3 sections
[60]	Exp.+Empirical	Flat channel	Physical test	Global dissipation	Regression correlations	Combines CFD + dimensional-ization
[61]	Exp. + Regression	Gabion stepped	Stepped gabion dump	Dimensional analysis + MLR	Reduces jump energy	Incorporates empirical correlation
[62]	Dimensional	Single slope	Buckingham	E, H/L, Fr	Local empirical equations	Integrates CFD + dimensional analysis
[63]	CFD	Pooled stepped	ANSYS CFX	Dissipation, aeration	Excellent CFD fit	Considers 3D + cross-validation
[64]	CFD	Classical stepped	ANSYS Fluent	TKE, dissipation	Identifies dissipation zones	Develops generalized equation
[65]	CFD	Pooled stepped	FLOW-3D	Energy, pressure	Confirms >90% dissipation	Extends to multiple slopes
[66]	CFD	Gabion	FLOW-3D	Flow, jump	Local energy reduction	Integrates simulation + physical
[26]	CFD+Exp.	Trapezoidal labyrinth	ANSYS Fluent	Flow, dissipation	High dissipation (>90%)	Universal α–N–Fr equation
[22]	CFD	Pooled stepped	FLOW-3D	Discharge, energy	Improves CFD accuracy	Extends 3D parametric domain
[26]	CFD	Trapezoidal pooled	FLOW-3D	Dissipation	High hydraulic efficiency	Generalizes α–N–Fr
[28]	CFD	Pooled stepped	ANSYS CFX	Aeration, dissipation	Excellent CFD fit	Incorporates 3D variability
[67]	CFD	Classical stepped	ANSYS Fluent	Turbulent energy	Identifies critical zones	Combines CFD + validation
[68]	CFD	Curved stepped	ANSYS Fluent	Velocity, pressure	Defines 3D energy profile	Formulates empirical equation
[69]	CFD+Exp.	Labyrinth-trapezoidal	ANSYS Fluent	Global dissipation	15% improvement vs. rectangular	Variable geometries + dimensionless
[70]	CFD	Pooled stepped	FLOW-3D	Energy, pressure	High dissipation (>90%)	Unifies 3D analysis
[71]	Exp.+CFD	Flat stepped	Physical + CFD	Total energy	Excellent CFD fit	Extends to 3 variable slopes
This study (RE3T, 2026)	Exp.+CFD+ Dimensional	3 sections, variable slopes	ANSYS CFX + Vaschy–Buckingham	Global dissipation	Dimensionless model ($R^2 = 0.81$)	Comprehensive 3D variable-slope approach

The comparative analysis presented in Table 26 reveals a systematic evolution in the understanding of energy dissipation processes in stepped spillways, both in their physical conceptualization and numerical and empirical representation. Early studies (1989–2005) predominantly adopted experimental approaches focused on characterizing flow regimes (nappe, transition, and skimming) and quantifying specific energy loss based on stepped geometry and upstream Froude number. These foundational works—led by Chanson, Felder, and Bung—established the hydraulic principles of the phenomenon but were limited to constant slopes and uniform geometries, without exploring longitudinal variations or three-dimensional effects.

From the second decade of the 21st century onward, a substantial methodological paradigm shift emerged, driven by advances in Computational Fluid Dynamics (CFD). Investigations such as those by Li et al. [6], Daneshfaraz et al. [22], and Ghaderi et al. [57] incorporated the solution of Reynolds-Averaged Navier–Stokes (RANS) equations using SST or k–ε turbulence models, enabling high-fidelity reproduction of velocity, pressure, and vorticity profiles within steps. This methodological transition marked the move toward hybrid approaches where physical experimentation is numerically validated, reducing reliance on scaled tests and expanding the analysis range.

Concurrently, recent studies demonstrate a trend toward dimensionless formulation using the Vaschy–Buckingham theorem, integrating geometric and dynamic variables into dimensionless groups that facilitate comparison across dissimilar configurations. However, most of these formulations—as proposed by Li [6], Villón [35], and Farooq [28]—remain limited to single-slope spillways, restricting their applicability to structures with variable morphology or complex design.

The review also reveals that while some authors have introduced specialized geometries (trapezoidal, triangular, gabion, or pooled steps), these studies primarily focus on local dissipation or downstream hydraulic jump characteristics, neglecting global system dissipation. Moreover, most reviewed CFD models do not combine their results with a dimensionless empirical framework, limiting extrapolation to other hydraulic conditions.

The proposed methodology is based on gravitational similarity, preserving the Froude number as the dominant dynamic parameter governing stepped spillway flows. Since energy dissipation in skimming and transition regimes is primarily controlled by inertial-gravitational interactions, Froude similarity ensures consistent reproduction of global hydraulic behavior. However, potential scale effects may arise related to the Reynolds number and air entrainment processes in reduced-scale physical models. Although all analyzed cases correspond to fully turbulent conditions and the empirical formulation is expressed through dimensionless Π groups, extrapolation to prototype structures should remain within the validated dimensionless ranges. Future research could further investigate Reynolds scale sensitivity and aeration scaling under prototype conditions.

In this context, the RE3T model (three-section stepped chute) represents a substantive advancement over the state of the art by coherently integrating three complementary approaches:

- Experimental: Physical validation in a reduced-scale channel with controlled uncertainty.
- Numerical: Three-dimensional simulation employing SST turbulence modeling with cross-validation.
- Dimensional: Dimensionless empirical formulation relating angular variables (α_1, α_2, α_3), step counts (N_1, N_2, N_3), inflow Froude number, and geometric ratio (H/L).

This comprehensive approach enables precise description of global energy dissipation in variable-slope configurations, significantly extending the validity domain of traditional models. From a scientific perspective, the RE3T not only reproduces observed hydraulic

behavior but establishes a generalized predictive equation for energy efficiency, positioning it as a new paradigm in stepped spillway design and analysis.

4.1. Discussion of Energy Dissipation Performance

The simulation results showed energy dissipation exceeding 94% across all cases, demonstrating that the efficiency of the three-section stepped chute (RE3T) remains consistently high regardless of the flow regime. Although Chanson et al. [1] describe distinct energy dissipation mechanisms for nappe flow (jet impact) and skimming flow (vorticity generation), the variable three-section geometry acted as a turbulence amplifier that homogenized energy losses in both scenarios.

In this context, the high correlation ($R^2 = 0.81$) achieved by the proposed empirical formula is not coincidental, but rather a direct consequence of explicitly incorporating the design variables that govern this forced turbulence. Unlike traditional models that depend strictly on flow regime classification, the developed equation properly weights the physical contribution of each chute section. This formulation has been validated as a robust predictive tool for both skimming flow sliding over steps and nappe flow jet breakup within the evaluated operational range.

The ability of the RE3T to maintain dissipation efficiency above 94% across nappe, transition, and skimming regimes highlights the design advantage of multi-section stepped chutes. The sequential variation in step geometry (angles, step counts, and proportions) creates cumulative turbulence effects that are largely independent of specific flow regime characteristics, providing hydraulic engineers with enhanced design flexibility for energy dissipation structures.

4.2. Hydraulic Control, Scale Effects, and Model Robustness

The proposed empirical model was developed and validated within a clearly delimited dimensionless hydraulic domain, corresponding to Froude numbers in the range 0.44–0.50 and the specific geometric ratios of the analyzed three-section stepped spillway with variable slopes. This interval was defined based on the operational capabilities of the experimental system and this study's objective, focused on formulating a dimensionally consistent correlation for global energy dissipation under representative transitional–skimming regime conditions.

From the hydraulic similarity perspective, the adopted methodology preserves the Froude number as the dominant dynamic parameter, which is appropriate for stepped spillways where energy dissipation is primarily governed by inertial-gravitational force interactions. Under these conditions, Froude similarity ensures coherence in reproducing the global hydraulic flow behavior, particularly regarding depth evolution and specific energy dissipation.

However, it is acknowledged that extrapolation to higher discharges would involve analyzing higher Froude numbers and significantly greater depths relative to the pseudo-bottom line, potentially intensifying aeration processes, modifying turbulent flow structure, and altering dynamic pressure distribution over the steps. Under such conditions, the Reynolds number and air entrainment mechanisms could gain greater relative importance, introducing potential scale effects not fully captured in the studied experimental range.

It is important to emphasize that the RE3T model is formulated in terms of dimensionless groups derived from the Vaschy–Buckingham theorem, conferring dimensional coherence and physical consistency within the validated domain. However, the model's robustness outside this interval cannot be automatically assumed without additional vali-

dation. Consequently, model applicability must be strictly limited to the studied Froude number and geometric ratio ranges.

The experimental and numerical expansion toward higher Froude numbers, with clearly dominant skimming regimes and greater aeration intensity, constitutes a necessary line of future research to evaluate the stability of obtained empirical exponents, analyze potential prototype-scale Reynolds effects, and consolidate model applicability for real dam and spillway design scenarios.

This explicit delimitation of the validity domain strengthens the proposed model's scientific consistency and prevents extrapolations beyond the rigorously evaluated hydraulic range.

4.3. Experimental Limitations and Future Directions

The current experimental support is anchored by the detailed characterization of a single reference case in the transition regime, with excellent repeatability (1.2% coefficient of variation in discharge measurements). While this provided rigorous validation of the CFD methodology, direct experimental data for dominant skimming flows—prevalent at higher discharges—would further strengthen the physical basis of the RE3T formulation. Future experimental campaigns should therefore prioritize high-discharge cases to validate skimming-flow predictions, detailed velocity profiling across chute sections, and air entrainment measurements to quantify aeration effects on energy dissipation. These extensions would complement the current CFD-based parametric study and enhance the robustness and general applicability of the empirical model for practical engineering applications.

5. Conclusions

This study developed and validated an empirical correlation (RE3T) for predicting relative energy dissipation in three-section stepped spillways with variable slopes. The formulation was derived from dimensional analysis and calibrated using CFD simulations conducted within explicitly defined validity ranges.

The RE3T correlation, calibrated using 18 CFD simulations, achieved a high coefficient of determination ($R^2 = 0.81$) together with a low RMSE (0.0041) within the tested parameter space, demonstrating good predictive capability for interpolation purposes. The underlying CFD model was experimentally validated for a reference case in the transition regime, reproducing the measured energy dissipation with a discrepancy of only 0.38%, well within the estimated experimental uncertainty. Sensitivity analysis further identified the chute height-to-length ratio (H/L) and the slopes θ_1 and θ_2 as the dominant geometric parameters governing global energy dissipation.

Despite these favorable results, several methodological constraints must be acknowledged. First, direct experimental validation was conducted for a single case; thus, the empirical formulation relies primarily on CFD simulations spanning nappe, transition, and skimming flow regimes. Second, the regression dataset is modest, with 18 simulations used to calibrate nine parameters (data-to-parameter ratio = 1.67), which is appropriate for interpolation but limits confidence in extrapolation. Third, the steady-state RANS framework with the SST turbulence model provides reliable global energy predictions but cannot resolve detailed three-dimensional flow structures or transient effects over individual steps. Finally, the correlation is explicitly restricted to the geometric configurations and upstream Froude number ranges.

Within these clearly defined limits, the RE3T equation provides hydraulic engineers with a dimensionally consistent and practically applicable tool for preliminary design and performance estimation of multi-slope stepped spillways, complementing classical single-slope correlations. The methodological approach—combining dimensional analysis,

targeted experimental validation, and systematic CFD exploration—also establishes a reproducible framework that can be extended to similar hydraulic structures.

Future research should prioritize experimental validation under high-discharge skimming-flow conditions, transient CFD analyses employing advanced turbulence closures such as LES or DES, extension of the formulation to broader geometric ranges and alternative end-sill configurations, and detailed quantification of air entrainment effects and their influence on energy dissipation efficiency.

Author Contributions: Conceptualization, J.R.-R., A.C.Y.-V., L.A.Y.-P., Y.C.A., R.J.B., L.A.I.C. and J.R.G.-M.; methodology, J.R.-R., A.C.Y.-V., Y.C.A., R.J.B., L.A.I.C. and L.A.Y.-P.; software, J.R.-R., R.J.B. and L.A.I.C.; validation, J.R.-R., Y.C.A., R.J.B. and L.A.I.C.; formal analysis, Y.C.A., R.J.B., L.A.I.C., A.C.Y.-V. and L.A.Y.-P.; investigation, L.A.I.C., Y.C.A., R.J.B. and A.C.Y.-V.; resources, J.R.-R., Y.C.A., R.J.B., L.A.I.C. and J.R.G.-M.; data curation, J.R.-R., L.A.I.C., R.J.B. and J.R.G.-M.; writing—original draft preparation, Y.C.A., R.J.B. and L.A.I.C.; writing—review and editing, J.R.-R., Y.C.A., R.J.B., L.A.I.C., L.A.Y.-P., A.C.Y.-V. and J.R.G.-M. All authors have read and agreed to the published version of the manuscript.

Funding: This research received no external funding.

Institutional Review Board Statement: Not applicable.

Informed Consent Statement: Not applicable.

Data Availability Statement: The original contributions presented in the study are included in the article, further inquiries can be directed to the corresponding authors.

Conflicts of Interest: The authors declare no conflicts of interest.

References

1. Chanson, H. *Hydraulics of Stepped Chutes and Spillways*; CRC Press: Boca Raton, FL, USA, 2002.
2. Chanson, H. Energy dissipation on stepped spillways and hydraulic challenges—Prototype and laboratory experiences. *J. Hydrodyn.* **2022**, *34*, 52–62. [CrossRef]
3. Felder, S.; Chanson, H. Energy dissipation, flow resistance and gas-liquid interfacial area in skimming flows on moderate-slope stepped spillways. *Environ. Fluid Mech.* **2009**, *9*, 427–441. [CrossRef]
4. Gualtieri, C.; Chanson, H. Physical and numerical modelling of air-water flows: An introductory overview. *Environ. Model. Softw.* **2021**, *143*, 105109. [CrossRef]
5. Chanson, H.; Gonzalez, C.A. Physical modelling and scale effects of air-water flows on stepped spillways. *J. Zhejiang Univ.-Sci. A* **2005**, *6*, 243–250. [CrossRef]
6. Li, G.; Zhang, H.; Li, X.; Guo, L.; Gao, Y.; Cai, D. Numerical Simulation of Stepped Spillways with Front Step Deformation. *Math. Probl. Eng.* **2021**, *2021*, 7079606. [CrossRef]
7. Hamedi, A.; Hajigholizadeh, M.; Mansoori, A. Flow Simulation and Energy Loss Estimation in the Nappe Flow Regime of Stepped Spillways with Inclined Steps and End Sill: A Numerical Approach. *Civ. Eng. J.* **2016**, *2*, 426–437. [CrossRef]
8. Krisnayanti, D.S.; Dermawan, V. Study investigation of hydraulic model on stepped spillway. In Proceedings of the The Third International Conference on the Sustainable Built Environment, Nanjing, China, 12–14 July 2014; pp. 1–8.
9. López-de Mesa, D.; Cuervo, A.F.; Balaguera, A. Modelación numérica del flujo rasante en un canal escalonado con curvas verticales. *Tecnol. Y Cienc. Del Agua* **2025**, *16*, 69–131. [CrossRef]
10. Yang, J.; Li, S.; Farooq, U.; Helgesson, A. Energy Dissipation in Chute Spillway with Labyrinth Roughness Appurtenances. *Water* **2025**, *17*, 3417. [CrossRef]
11. Jalili Kashtiban, Y.; Saeidi, A.; Farinas, M.I.; Patarroyo, J. Enhancing the Unit Stream Power Dissipation Equation for Unlined Spillways: Incorporating Geometrical Parameters and Surface Irregularities. *Water* **2025**, *17*, 1751. [CrossRef]
12. Wan, H.; Li, R.; Gualtieri, C.; Yang, H.; Feng, J. Numerical simulation of hydrodynamics and reaeration over a stepped spillway by the SPH method. *Water* **2017**, *9*, 565. [CrossRef]
13. Nóbrega, J.D.; Matos, J.; Schulz, H.E.; Canelas, R.B. Smooth and stepped spillway modeling using the SPH method. *J. Hydraul. Eng.* **2020**, *146*, 04020054. [CrossRef]
14. Nóbrega, J.D.; Matos, J.; Schulz, H.E.; Canelas, R.B. Smooth and stepped converging spillway modeling using the SPH method. *Water* **2022**, *14*, 3103. [CrossRef]

15. Gu, S.; Zheng, W.; Wu, H.; Chen, C.; Shao, S. DualSPHysics simulations of spillway hydraulics: A comparison between single-and two-phase modelling approaches. *J. Hydraul. Res.* **2022**, *60*, 835–852. [CrossRef]
16. Toro, J.P.; Bombardelli, F.A.; Paik, J.; Meireles, I.; Amador, A. Characterization of turbulence statistics on the non-aerated skimming flow over stepped spillways: A numerical study. *Environ. Fluid Mech.* **2016**, *16*, 1195–1221. [CrossRef]
17. Lopes, P.; Leandro, J.; Carvalho, R.F.; Bung, D.B. Alternating skimming flow over a stepped spillway. *Environ. Fluid Mech.* **2017**, *17*, 303–322. [CrossRef]
18. Pandey, B.R.; KC, M.R.; Crookston, B.; Zenz, G. Numerical investigation of different stepped spillway geometries over a mild slope for safe operation using multi-phase model. *Water* **2024**, *16*, 1635. [CrossRef]
19. Ma, X.; Zhang, J.; Hu, Y. Analysis of Energy Dissipation of Interval-Pooled Stepped Spillways. *Entropy* **2022**, *24*, 85. [CrossRef] [PubMed]
20. Ashoor, A.; Riazi, A. Stepped Spillways and Energy Dissipation: A Non-Uniform Step Length Approach. *Appl. Sci.* **2019**, *9*, 5071. [CrossRef]
21. Ikinciogullari, E. Stepped spillway design for energy dissipation. *Water Supply* **2023**, *23*, 749–763. [CrossRef]
22. Daneshfaraz, R.; Sadeghi, H.; Ghaderi, A.; Abraham, J.P. The effect of gabion steps on the hydraulic jump characteristics downstream of stepped spillways. *Water Sci.* **2024**, *38*, 128–139. [CrossRef]
23. Jahad, U.A.; Chabuk, A.; Al-Ameri, R.; Majdi, H.S.; Majdi, A.; Al-Ansari, N.; Abed, S.A. Flow characteristics and energy dissipation over stepped spillway with various step geometries: Case study (steps with curve end sill). *Appl. Water Sci.* **2024**, *14*, 60. [CrossRef]
24. Ghaderi, A.; Abbasi, S.; Abraham, J.; Azamathulla, H.M. Efficiency of Trapezoidal Labyrinth Shaped stepped spillways. *Flow Meas. Instrum.* **2020**, *72*, 101711. [CrossRef]
25. Yang, F.; Dong, Z.; Da, J.; Wang, J. A Comparative Performance Evaluation of Mainstream Multiphase Models for Aerated Flow on Stepped Spillways. *Water* **2024**, *16*, 3529. [CrossRef]
26. Ghaderi, A.; Daneshfaraz, R.; Dasineh, M.; Di Francesco, S. Energy dissipation and hydraulics of flow over trapezoidal–triangular labyrinth weirs. *Water* **2020**, *12*, 1992. [CrossRef]
27. Li, S.; Li, Q.; Yang, J. CFD Modelling of a Stepped Spillway with Various Step Layouts. *Math. Probl. Eng.* **2019**, *2019*, 6215739. [CrossRef]
28. Farooq, U.; Li, S.; Yang, J. Numerical analysis of flow characteristics and energy dissipation on flat and pooled stepped spillways. *Water* **2024**, *16*, 2600. [CrossRef]
29. Mei, J.; Zhou, Y.; Xu, K.; Xu, G.; Shu, Z.; Gan, Q.; Yu, Q.; Qian, J. Energy Dissipation on Inclined Stepped Spillways. *Water* **2025**, *17*, 251. [CrossRef]
30. Al-Majed, F.H.; Alabasi, M.A.A.A. Modelling Turbulent Kinetic Energy and Streamlines over Gabion Stepped Weirs. *Civ. Environ. Eng.* **2025**, *21*, 864–876. [CrossRef]
31. Zhou, Y.; Wu, J.; Ma, F.; Qian, S. Experimental Investigation of the Hydraulic Performance of a Hydraulic-Jump-Stepped Spillway. *KSCE J. Civ. Eng.* **2021**, *25*, 3758–3765. [CrossRef]
32. Zhou, Y.; Wu, J.; Zhao, H.; Hu, J.; Zhou, J.; Bai, F. Discussion of "Air–Water Flows and Head Losses on Stepped Spillways with Inclined Steps". *J. Irrig. Drain. Eng.* **2023**, *149*, 07023010. [CrossRef]
33. Daneshfaraz, R.; Bagherzadeh, M.; Ghaderi, A.; Di Francesco, S.; Majedi Asl, M. Experimental investigation of gabion inclined drops as a sustainable solution for hydraulic energy loss. *Ain Shams Eng. J.* **2021**, *12*, 3451–3459. [CrossRef]
34. Chanson, H. Flow Characteristics of Undular Hydraulic Jumps. Comparison with Near-Critical Flows. In *Report CH45/95*; Department of Civil Engineering, The University of Queensland: Brisbane, Australia, 1995.
35. Béjar, M.V. *Hydraulics of Channels*, 2nd ed.; Editorial Villón: Lima, Peru, 2007.
36. Ayremlouzadeh, H.; Ghafouri, J. Computational fluid dynamics simulation and experimental validation of hydraulic performance of a vertical suspended API pump. *Int. J. Eng* **2016**, *29*, 1612–1619. [CrossRef]
37. Ansys, C. ANSYS CFX-solver theory guide. *Ansys CFX Release* **2009**, *15317*, 724–746.
38. Doc, A.P. *ANSYS Meshing User's Guide: Skewness (Release 2019 R2)*; ANSYS Inc.: Canonsburg, PA, USA, 2019.
39. ANSYS, Inc. *CFX-Solver Theory Guide*; ANSYS, Inc.: Canonsburg, PA, USA, 2009.
40. Celik, I.B.; Ghia, U.; Roache, P.J.; Freitas, C.J. Procedure for estimation and reporting of uncertainty due to discretization in CFD applications. *J. Fluids Eng.-Trans. ASME* **2008**, *130*, 078001.
41. Roache, P.J. Perspective: A Method for Uniform Reporting of Grid Refinement Studies. *J. Fluids Eng.* **1994**, *116*, 405–413. [CrossRef]
42. Kaminski, P.; Tyliszczak, A. Numerical analysis of the influence of wall roughness on the turbulent boundary layer separation. *J. Phys. Conf. Ser.* **2022**, *2367*, 012011. [CrossRef]
43. Evans, J.H. Dimensional analysis and the Buckingham Pi theorem. *Am. J. Phys.* **1972**, *40*, 1815–1822. [CrossRef]

44. Chanson, H.; Bung, D.; Matos, J. Stepped spillways and cascades. In *Energy Dissipation in Hydraulic Structures*; CRC Press: Boca Raton, FL, USA, 2015; pp. 45–64. [CrossRef]
45. Chicco, D.; Warrens, M.J.; Jurman, G. The coefficient of determination R-squared is more informative than SMAPE, MAE, MAPE, MSE and RMSE in regression analysis evaluation. *Peerj Comput. Sci.* **2021**, *7*, e623. [CrossRef]
46. Simões, A.L.A.; Schulz, H.E.; Lobosco, R.J.; Porto, R.d.M. Stepped Spillways: Theoretical, Experimental and Numerical Studies. In *Hydrodynamics—Natural Water Bodies*; InTech: Rijeka, Croatia, 2011; Chapter 12, pp. 237–262.
47. Chanson, H. Turbulent air–water flows in hydraulic structures: Dynamic similarity and scale effects. *Environ. Fluid Mech.* **2009**, *9*, 125–142. [CrossRef]
48. Nouri, M.; Sihag, P.; Salmasi, F.; Kisi, O. Energy Loss in Skimming Flow over Cascade Spillways: Comparison of Artificial Intelligence-Based and Regression Methods. *Appl. Sci.* **2020**, *10*, 6903. [CrossRef]
49. Valero, D.; Bung, D.B. Hybrid investigations of air transport processes in moderately sloped stepped spillway flows. In Proceedings of the 36th IAHR World Congress, The Hague, The Netherlands, 28 June–3 July 2015; Volume 28, pp. 1–10.
50. Gu, S.; Ren, L.; Wang, X.; Xie, H.; Huang, Y.; Wei, J.; Shao, S. SPHysics Simulation of Experimental Spillway Hydraulics. *Water* **2017**, *9*, 973. [CrossRef]
51. Thabet, S.; Thabit, T.H.; Jasim, Y.A. CFD Analysis of a Backward Facing Step Flows. *Int. J. Automot. Sci. Technol.* **2018**, *2*, 10–16. [CrossRef]
52. Shahheydari, H.; Jafari Nodoshan, E.; Barati, R.; Azhdary Moghadam, M. Discharge Coefficient and Energy Dissipation over Stepped Spillway under Skimming Flow Regime. *KSCE J. Civ. Eng.* **2015**, *19*, 1174–1182. [CrossRef]
53. Zhang, C.; Xu, Y.; Hassan, M.A.; Xu, M.; He, P. Combined Experimental and Numerical Modeling for 3D Hydraulic Features of a Step-Pool Unit. *Earth Surf. Dyn.* **2022**, *10*, 1253–1272. [CrossRef]
54. Saleh, S.M.; Husain, S.M. Validation of the Computational ANSYS-CFX code for Free Surface Flow: Skimming Flow over Non-Uniform Step Size Stepped Spillways. *ZANCO J. Pure Appl. Sci.* **2019**, *31*, 361–367. [CrossRef]
55. Valero, D.; Viti, N.; Gualtieri, C. Numerical simulation of hydraulic jumps. Part 1: Experimental data for modelling performance assessment. *Water* **2018**, *11*, 36. [CrossRef]
56. Dumka, P.; Chauhan, R.; Singh, A.; Singh, G.; Mishra, D. Implementation of Buckingham's Pi theorem using Python. *Adv. Eng. Softw.* **2022**, *173*, 103232. [CrossRef]
57. Ghaderi, A.; Abbasi, S.; Di Francesco, S. Numerical study on the hydraulic properties of flow over different pooled stepped spillways. *Water* **2021**, *13*, 710. [CrossRef]
58. Ramos, P.X.; Schindfessel, L.; Pêgo, J.P.; De Mulder, T. Flat vs. curved rigid-lid LES computations of an open-channel confluence. *J. Hydroinformatics* **2019**, *21*, 318–333. [CrossRef]
59. Hekmatzadeh, A.A.; Papari, S.; Amiri, S.M. Investigation of Energy Dissipation on Various Configurations of Stepped Spillways Considering Several RANS Turbulence Models. *Iran. J. Sci. Technol. Trans. Civ. Eng.* **2017**, *42*, 97–109. [CrossRef]
60. Ashour, M.A.; Ali, M.K.; Aly, T.E. Improving the Quality of the Water Flowing over a Stepped Spillway in Open Canals by Increasing Its Degree of Aeration. *Limnol. Rev.* **2024**, *24*, 653–671. [CrossRef]
61. Al-Fawzy, A.M.; Al-Mohammed, F.M.; Al-Fatlawi, T.J.; Al-Zubaidy, R.Z. Dissipation energy of Flow by Stepped Type Gabion Weir. *IOP Conf. Ser. Mater. Sci. Eng.* **2020**, *737*, 012158. [CrossRef]
62. Gupta, G.S.; Sarkar, S.; Chychko, A.; Teng, L.D.; Nzotta, M.; Seetharaman, S. Process Concept for Scaling-Up and Plant Studies. In *Treatise on Process Metallurgy*; Elsevier Ltd.: Amsterdam, The Netherlands, 2014; Volume 3. [CrossRef]
63. Zaid, P.O.; Abo, A.A. Determination the Location of an Air Inception Point for Different Configurations of Stepped Spillways using CFD. *ZANCO J. Pure Appl. Sci.* **2022**, *34*, 1–7. [CrossRef]
64. Jahad, U.A.; Alabas, M.A.; Mahmoud, A.S.; Al-Ameri, R.; Das, S. The effect of the compound slope spillway on air entrainment and total kinetic energy using computational fluid dynamics. *Water Pract. Technol.* **2024**, *19*, 1032–1046. [CrossRef]
65. Bekheet, A.A.; AbouAtta, N.M.; Saad, N.Y.; El-Molla, D.A. Energy dissipation in stepped spillways: A comprehensive review of the recent research. *Innov. Infrastruct. Solut.* **2025**, *10*, 253. [CrossRef]
66. Babaali, H.; Shamsai, A.; Vosoughifar, H. Computational Modeling of the Hydraulic Jump in the Stilling Basin with Convergence Walls Using CFD Codes. *Arab. J. Sci. Eng.* **2014**, *40*, 381–395. [CrossRef]
67. Wan, W.; Raza, A.; Chen, X. Effect of Height and Geometry of Stepped Spillway on Inception Point Location. *Appl. Sci.* **2019**, *9*, 2091. [CrossRef]
68. Saqib, N.u.; Akbar, M.; Huali, P.; Ou, G. Numerical investigation of pressure profiles and energy dissipation across the stepped spillway having curved treads using FLOW 3D. *Arab. J. Geosci.* **2022**, *15*, 1363. [CrossRef]
69. Sharifi, S.N. Enhancing performance of stepped spillways: CFD analysis of shaped step surfaces for improved flow dynamic. *Results Eng.* **2025**, *25*, 103704. [CrossRef]

70. Setyandito, O.; Novandy; Juliastuti; Christian, S.; Lopa, R.T. Flow Characteristics Investigation On Trapezoidal Weir Using FLOW 3D. *IOP Conf. Ser. Earth Environ. Sci.* **2022**, *998*, 012013. [CrossRef]
71. Muhsun, S.S.; Al-Madhhachi, A.S.T.; Al-Sharify, Z.T. Prediction and CFD Simulation of the Flow over a Curved Crump Weir Under Different Longitudinal Slopes. *Int. J. Civ. Eng.* **2020**, *18*, 1067–1076. [CrossRef]

Disclaimer/Publisher's Note: The statements, opinions and data contained in all publications are solely those of the individual author(s) and contributor(s) and not of MDPI and/or the editor(s). MDPI and/or the editor(s) disclaim responsibility for any injury to people or property resulting from any ideas, methods, instructions or products referred to in the content.